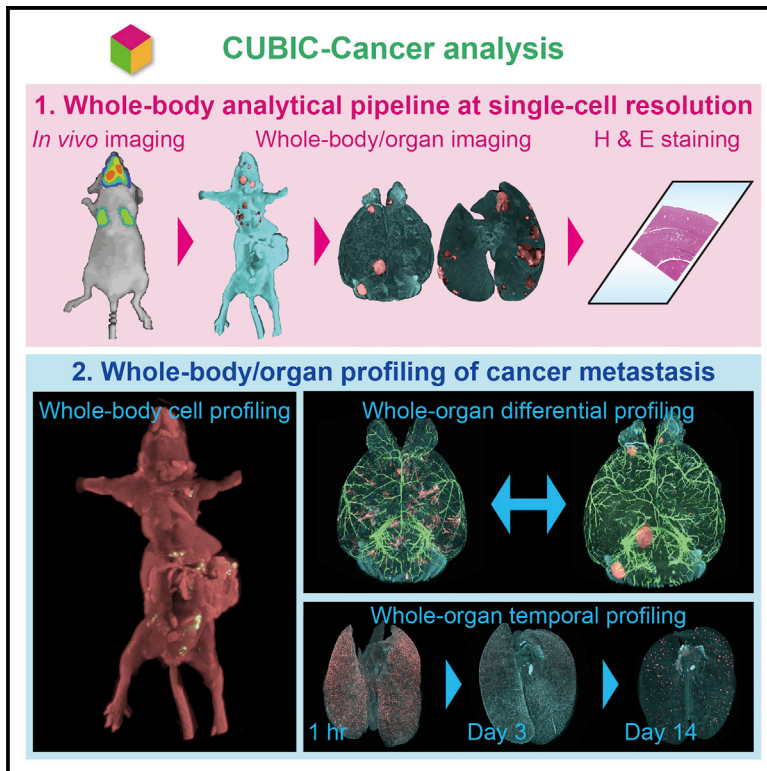


Cell Reports

Whole-Body Profiling of Cancer Metastasis with Single-Cell Resolution

Graphical Abstract



Authors

Shimpei I. Kubota, Kei Takahashi, Jun Nishida, ..., Kazuki Tainaka, Kohei Miyazono, Hiroki R. Ueda

Correspondence

miyazono@m.u-tokyo.ac.jp (K.M.), uedah-ky@umin.ac.jp (H.R.U.)

In Brief

Kubota et al. find that CUBIC-cancer analysis can profile cancer metastasis at a single-cell level in a whole-animal context. In addition, CUBIC-cancer analysis can bridge the resolution gap between *in vivo* bioluminescence imaging and histology. This analytical pipeline would contribute to the profiling of biological functions of whole organs.

Highlights

- RI-optimized CUBIC protocol enables whole-body examination of cancer models
- CUBIC is applicable to analysis of micrometastases at single-cell resolution
- CUBIC analysis bridges the resolution gap between *in vivo* imaging and histology
- CUBIC-cancer analysis is useful for profiling biological processes in whole organs



Whole-Body Profiling of Cancer Metastasis with Single-Cell Resolution

Shimpei I. Kubota,^{1,5} Kei Takahashi,^{2,5} Jun Nishida,² Yasuyuki Morishita,² Shogo Ehata,² Kazuki Tainaka,^{1,3} Kohei Miyazono,^{2,*} and Hiroki R. Ueda^{1,4,6,*}

¹Department of Systems Pharmacology, Graduate School of Medicine, The University of Tokyo, 7-3-1 Hongo, Bunkyo-ku, Tokyo 113-0033, Japan

²Department of Molecular Pathology, Graduate School of Medicine, The University of Tokyo, 7-3-1 Hongo, Bunkyo-ku, Tokyo 113-0033, Japan

³Brain Research Institute, Niigata University, 1-757 Asahimachidori, Chuo-ku, Niigata 951-8585, Japan

⁴Laboratory for Synthetic Biology, RIKEN Quantitative Biology Center, 1-3 Yamadaoka, Suita, Osaka 565-5241, Japan

⁵These authors contributed equally

⁶Lead Contact

*Correspondence: miyazono@m.u-tokyo.ac.jp (K.M.), uedah-ky@umin.ac.jp (H.R.U.)

<http://dx.doi.org/10.1016/j.celrep.2017.06.010>

SUMMARY

Stochastic and proliferative events initiated from a single cell can disrupt homeostatic balance and lead to fatal disease processes such as cancer metastasis. To overcome metastasis, it is necessary to detect and quantify sparsely distributed metastatic cells throughout the body at early stages. Here, we demonstrate that clear, unobstructed brain/body imaging cocktails and computational analysis (CUBIC)-based cancer (CUBIC-cancer) analysis with a refractive index (RI)-optimized protocol enables comprehensive cancer cell profiling of the whole body and organs. We applied CUBIC-cancer analysis to 13 mouse models using nine cancer cell lines and spatiotemporal quantification of metastatic cancer progression at single-cell resolution. CUBIC-cancer analysis suggests that the epithelial-mesenchymal transition promotes not only extravasation but also cell survival at metastatic sites. CUBIC-cancer analysis is also applicable to pharmacotherapeutic profiling of anti-tumor drugs. CUBIC-cancer analysis is compatible with *in vivo* bioluminescence imaging and 2D histology. We suggest that a scalable analytical pipeline with these three modalities may contribute to addressing currently incurable metastatic diseases.

INTRODUCTION

Rudolf Virchow, the father of modern pathology, declared that the body is a “cell state, in which every cell is a citizen” and disease is “merely a conflict of citizens in this state brought about by the action of external forces” (Nicholls, 1927). His cell theory brought the current concept of cellular pathology based on microscopic histological analysis to the early model of pathol-

ogy, which largely relied on clinical symptoms and gross appearances in patients. Thereafter, comprehensive analysis and decoding of the more than 100 billion cells comprising the mammalian body have become one of the ultimate goals in biology and medicine. Although recent advances in a series of live-imaging systems have provided important breakthroughs to examine dynamics at the whole-body scale, it is still difficult to clarify the generation and progression of diseases with stochastic and proliferative processes, such as autoimmune and malignant neoplastic diseases (Saadatpour et al., 2017; Takahashi et al., 2015). In particular, tumor metastasis can be initiated by a few cancer cells, and use of current imaging systems is a challenge due to their limited spatial resolution. Additionally, according to metastasis images from these imaging systems, 3D reconstitution of possibly affected organs by 2D histology is labor intensive. To bridge the spatial resolution gap between these approaches, a fundamentally novel analytical platform is required. To detect and quantify sparsely distributed metastatic cells at early stages of cancer metastasis, it is necessary to detect metastatic cells throughout the whole body and visualize individual tumor microenvironments.

Tissue-clearing-based 3D imaging is a most promising strategy for the visualization of the entire mouse body/organs at single-cell resolution (Susaki and Ueda, 2016). Recently, various kinds of tissue-clearing protocols have been developed, including organic solvent-based methods (Dodt et al., 2007; Ertürk et al., 2012; Renier et al., 2014), hydrophilic chemical-based methods (Cuccarese et al., 2017; Hama et al., 2011; Ke et al., 2013), and hydrogel-based methods (Chung et al., 2013). Spalteholz (1914) first established the basic concept of human tissue clearing based on organic solvents. Although tissue-clearing protocols have been available for a century, it is still difficult to comprehensively visualize sparsely distributed pathogenic cells throughout the mouse body using current tissue-clearing protocols.

In this study, we first investigate optimal refractive indices (RIs) ranging from 1.44 to 1.52 against each organ, and we demonstrate that an RI of 1.52 has the highest clearing efficiency among major organs. Then, we describe a highly efficient clearing

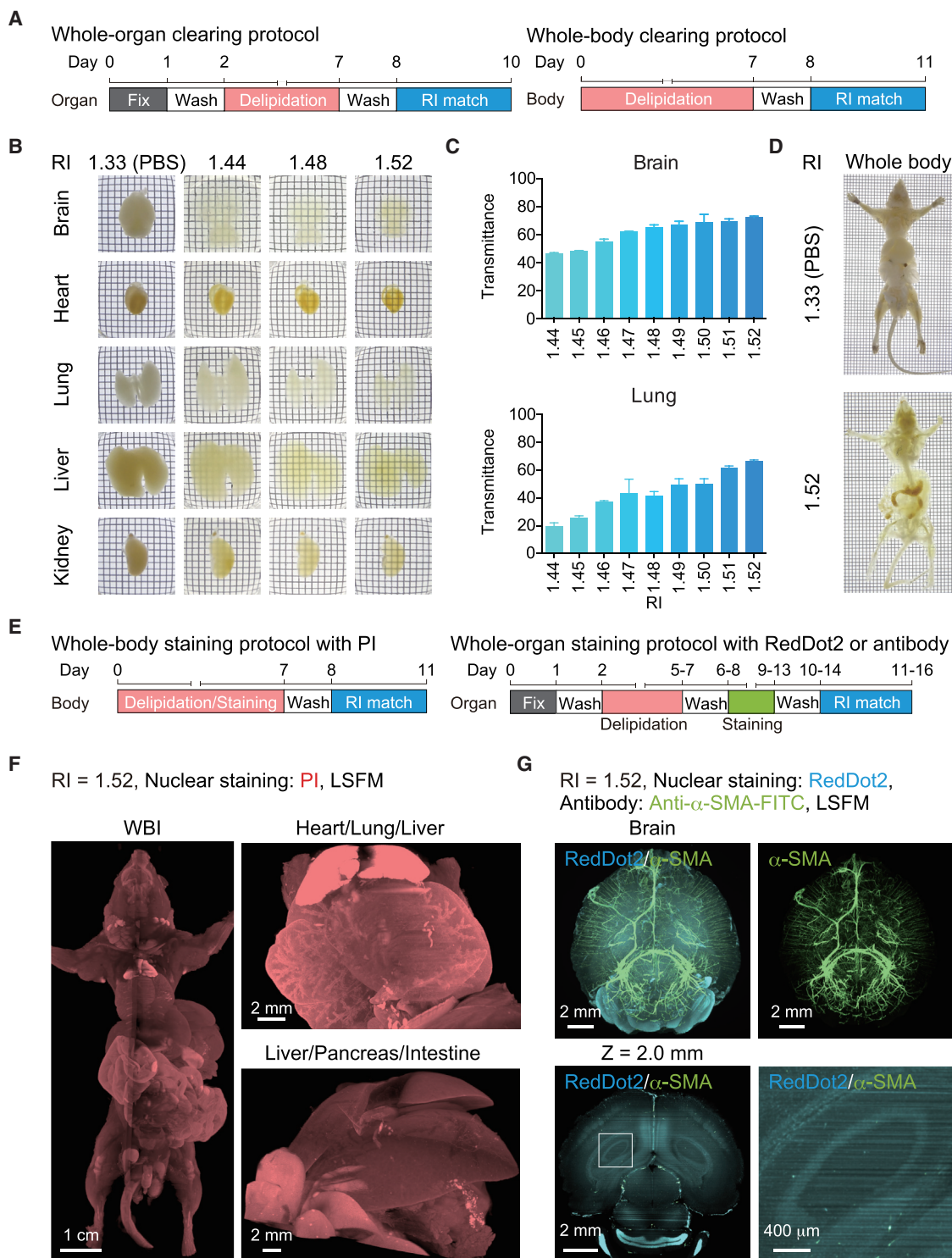


Figure 1. Whole-Body and Whole-Organ Clearing and Imaging with Optimized RI Solutions

(A) Whole-body and whole-organ clearing protocols. The whole-body clearing protocol (left) and the whole-organ clearing protocol (right) are shown. (B) Bright-field images of whole organs (brain, heart, lung, liver, and kidney) from C57BL/6N mouse (13 weeks old, male) after RI adjustment (RI = 1.44, 1.48, and 1.52). Control organs were stocked in PBS buffer (RI = 1.33). (C) Average parallel transmittance of RI-adjusted brain and lung. Parallel light transmittance around the visible region (450–750 nm) of organs was measured (n = 2). Data represent mean \pm SD.

(legend continued on next page)

protocol for the whole adult mouse body using a more efficient delipidation cocktail, clear unobstructed brain/body imaging cocktails and computational analysis (CUBIC)-L, and an optimized RI-matching medium, CUBIC-R. The specimens treated with this clearing protocol are clear enough to use for 3D imaging of the entire mouse body. The combination of light-sheet fluorescent microscopy (LSFM) and confocal laser-scanning microscopy (CLSM) enables the detection of cancer micrometastases in various kinds of mouse models. Our CUBIC-cancer analysis is compatible with the *in vivo* bioluminescence imaging system and conventional 2D histology, successfully bridging the spatial resolution gap between these approaches. CUBIC-cancer analysis is applied here to 13 mouse models using nine cancer cell lines, and it distinguishes different hematogenous metastatic patterns, such as angiogenic growth and co-optive growth. Moreover, CUBIC-cancer analysis enables the spatiotemporal quantification of metastatic cells even in the early stages of metastasis formation. In addition, we investigated the *in vivo* role of transforming growth factor β (TGF- β) signaling in lung metastasis, and we applied an *in vivo* system to evaluate the therapeutic effect of anti-cancer drugs on cancer metastasis. CUBIC-cancer analysis provides a fundamental platform for the analysis of the metastatic growth and progression of cancer throughout the body.

RESULTS

Optimized RI Cocktail Enables Whole-Body and Whole-Organ Clearing in Adult Mice

Previously, we achieved the whole-body imaging of postnatal day 1 mice at single-cell resolution by whole-body clearing based on a ScaleCUBIC-1 reagent (Tainaka et al., 2014). However, it remains difficult to sensitively and comprehensively detect the distribution of cancer cells that have metastasized to organs throughout the body of adult mice because of an insufficient delipidation efficiency and the unoptimized RI value of the ScaleCUBIC-1 reagent. To address these issues, we have performed comprehensive chemical profiling of hydrophilic chemicals to characterize highly effective delipidation reagents and water-soluble high-RI reagents (T.C. Murakami and K. Tainaka, unpublished data). Through a further combinatorial analysis, we identified the optimized cocktail of 10 w%/10 w% *N*-butyldiethanolamine/Triton X-100 (termed CUBIC-L) for delipidation. CUBIC-L enabled the complete delipidation of isolated paraformaldehyde (PFA)-fixed organs within 2 to 5 days, depending on the organ without pre-treatment with CUBIC-perfusion and quenching of proteins (Figure 1A, left). We found that CUBIC-L could also permeabilize skin-detached body samples of adult

mice using the CUBIC-perfusion protocol and subsequent delipidation for 7 days (Figure 1A, right; Supplemental Experimental Procedures).

As for the RI-matching step, there is an ongoing controversy about the most appropriate RI for permeabilized tissues (Tainaka et al., 2016). The RI for each intact biological tissue may depend on the contents and densities of lipids, proteins, and other constituents (Johnsen and Widder, 1999; Tuchin, 2015). Since hydrophilic RI media with an RI over 1.52 were likely to precipitate at room temperature, we evaluated RI-matching cocktails composed of antipyrine and nicotinamide with RIs ranging from 1.44 to 1.52 for clearing permeabilized major organs, considering practical use. After a 2-day treatment, all major organs appeared to be most efficiently transparentized by the RI-matching cocktail with an RI of 1.52 (Figures 1B and S1A), termed CUBIC-R, which is composed of 45 w%/30 w% antipyrine/nicotinamide. Indeed, the transmittance of the chemically treated organs increased as the RI value increased (Figures 1C and S1B). We noted that all organs treated with CUBIC-L and CUBIC-R showed significantly high transmittance in the 450 to 750 nm range, probably due to the high decoloring ability of *N*-butyldiethanolamine in CUBIC-L (Figure S1C). These results prompted us to render the whole-body clearing of adult mice using CUBIC-R (RI = 1.52) as a final RI-matching step. The transmission images of adult mice demonstrated that the new protocol markedly transparentized adult mice to visualize caudal vertebrae in ventral to dorsal (V-D) images (Figure 1D).

The New CUBIC Protocol Enables the Whole-Body and Whole-Organ Imaging of Adult Mice by 3D Nuclear Counterstaining and Immunohistochemistry

Simultaneous visualization of cancer cells, overall organ structures, and related molecular markers would facilitate our understanding of the underlying molecular mechanisms of cancer metastasis. For the comprehensive analysis of cancer metastasis, we initially carried out nuclear counterstaining with RedDot2 or propidium iodide (PI) to acquire whole-body and whole-organ structural images using LSFM according to our previous staining protocols (Figure 1E) (Susaki et al., 2014; Tatsuki et al., 2016). The resulting 3D-reconstituted image of each organ enabled the visualization of anatomical structural images even in deeper regions (Figure S1D). The new CUBIC protocol allowed the whole-body imaging of adult mice, clearly visualizing the internal structures of cardiovascular and abdominal organs (Figures 1F and S1E).

Next, we investigated whether the new CUBIC protocol is compatible with 3D immunohistochemistry. The brains of adult mice were co-stained with RedDot2 and anti- α -smooth muscle

(D) Bright-field images of whole body of C57BL/6N mouse (6 weeks old, male) treated with CUBIC-R. After delipidation and decolorization, adult mouse bodies were treated with PBS buffer (upper) or CUBIC-R (lower).

(E) Whole-body and whole-organ staining protocols. The whole-body staining protocol with PI (left) and the whole-organ staining protocol with RedDot2 or fluorescently labeled primary antibody (right) are shown.

(F) The 3D-reconstituted (3D) body images of PI-stained adult C57BL/6N mouse (10 weeks old, male). Whole-body imaging (WBI), thoracic organ imaging, and abdominal organ imaging are shown.

(G) The 3D-immunostained organ images. The brain from C57BL/6N mouse (15 weeks old, male) was stained with RedDot2 and fluorescein isothiocyanate (FITC)-conjugated anti- α -SMA antibody. 3D (upper) and x-y plane (XY) (lower) images are shown. The white inset was magnified next to the XY image. See also Figure S1.

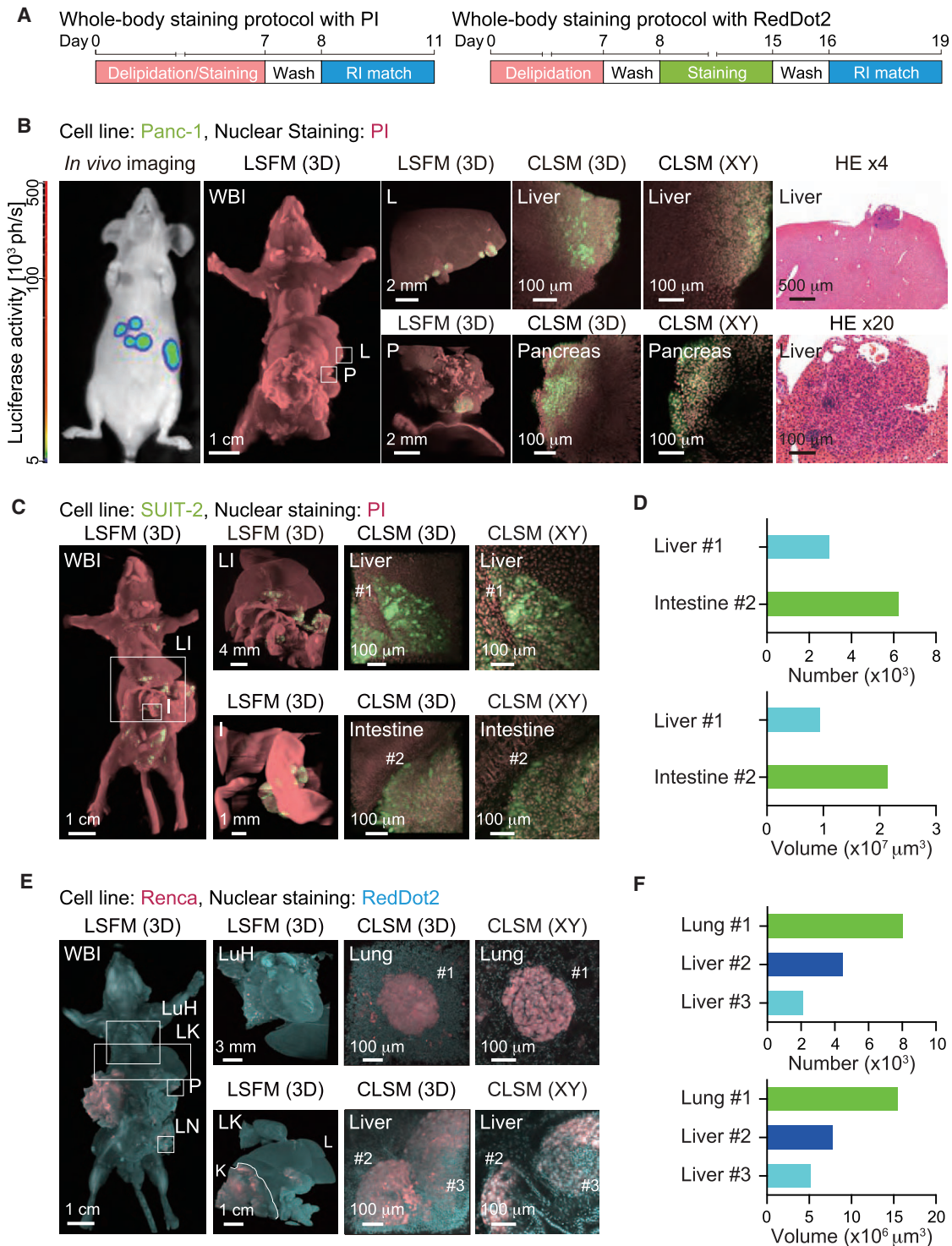


Figure 2. Whole-Body Imaging of Cancer Metastasis at Single-Cell Resolution

(A) Whole-body and whole-organ staining protocols. The whole-body staining protocol with PI (left) and the whole-body staining protocol with RedDot2 (right) are shown.

(B) Whole-body imaging of the experimental liver metastasis model by splenic injection with Panc-1 cells in BALB/c-*nu/nu* mice. The bioluminescence image (leftmost), WBI, images around the metastatic sites in the liver (L) and pancreas (P) with CUBIC-cancer analysis (second and third from left), magnified 3D and XY images (fourth and fifth from left) (Panc-1: GFP, nuclei: PI), and representative images of HE staining after CUBIC-cancer analysis (rightmost) are shown.

(legend continued on next page)

actin (α -SMA) antibody according to the staining protocol (Figures 1E and 1G). Spatial distributions of smooth muscle cells and lymphatic endothelial cells were simultaneously visualized in the lung by co-staining of α -SMA and vascular endothelial growth factor receptor 3 (VEGFR3) (Figure S1F). Hence, our CUBIC protocol was also applicable to 3D multiple immunohistochemical labeling. These results indicate that the new CUBIC protocol is a powerful tool for comprehensive pathological analysis.

CUBIC-Cancer Analysis Enables the Whole-Body Imaging of Cancer Metastasis at Single-Cell Resolution

To bridge the resolution gap between *in vivo* bioluminescence imaging and 2D histology with our scalable CUBIC-based cancer (CUBIC-cancer) analysis, we established cancer cells stably expressing firefly luciferase and fluorescence proteins, and we used them in mouse models (Figure 2A). First, we employed an experimental liver metastasis model by splenic injection of human pancreatic cancer cells (Panc-1). Nine weeks after injection, bioluminescence signals were detected in the abdomens of the mice (Figure 2B, left panel). We applied the CUBIC-cancer analysis and PI-staining protocol to this mouse model, and then we acquired whole-body images with LSFM (Figure 2A). As a result, fluorescence signals were successfully visualized in several organs, suggesting that the CUBIC-cancer analysis is applicable to the fluorescent proteins (Figure 2B, middle panels). In addition, magnified 3D images of these organs were obtained with CLSM in the CUBIC-cancer analysis. We noted that the resolution of these 3D images was high enough to discriminate individual cancer cells and comparable to that of 2D hematoxylin and eosin (HE) slice images, which were obtained after CUBIC-cancer analysis (Figure 2B, right panels).

As another pathway of cancer metastasis, peritoneal dissemination model mice were generated by the intraperitoneal injection of human pancreatic cancer cells (SUIT-2). Twenty-two days after injection, mCherry signals from SUIT-2 cells were observed in the liver and small intestine by CUBIC-cancer analysis (Figure 2C), roughly corresponding to those of bioluminescence signals from *in vivo* bioluminescence imaging (Figure S2A, left panel). Combined with counterstained confocal images, we succeeded in the direct quantification of the cell numbers of cancer colonies (Figures 2C and 2D). The CUBIC-cancer analysis also recapitulated cancer dissemination in other mice with SUIT-2 cells (Figures S2B and S2C), indicating the wide applicability of the CUBIC-cancer analysis protocol.

To prepare a syngeneic tumor model, we orthotopically injected murine renal cancer cells (Renca) into wild-type BALB/c

mice. Although the formation of a primary renal tumor was visualized 2 weeks after injection, it was difficult to detect cancer metastasis to other organs by *in vivo* bioluminescence imaging (Figure S2A, right panel). In contrast, CUBIC-cancer analysis revealed that numerous metastatic colonies had widely spread to the lung, liver, pancreas, and mesenteric lymph nodes (Figures 2E and S2D). Using CUBIC-cancer analysis combined with LSFM and CLSM, we also succeeded in the direct quantification of the cell numbers of these dispersed metastatic colonies (Figures 2F and S2E). Taken together, CUBIC-cancer analysis makes it possible to not only detect the dispersion of metastatic cancer cells throughout the entire body with high sensitivity but also determine the spatial distribution of individual cancer cells at single-cell resolution. In addition, CUBIC-cancer analysis is compatible with *in vivo* bioluminescence imaging and 2D histology.

Whole-Organ CUBIC-Cancer Analysis Provides a Systematic, Robust, Widely Applicable, and Immunolabeling-Compatible Analytical Platform for Cancer Metastasis

After the comprehensive detection of cancer metastasis throughout the body, the whole-organ CUBIC-cancer analysis would globally delineate the metastatic landscape of each cancer metastasis model. To this end, whole-organ clearing and staining were conducted according to Figure 3A. Initially, we quantified the growth of primary tumors in orthotopic models with SUIT-2 cells and OS-RC-2 cells (Figure S3A). CUBIC-cancer analysis also permitted us to visualize metastatic colonies in whole organs, including the lung, liver, and intestine (Figure 3B). The colony number and volume of the metastasis in each organ were calculated (Figure S3B). We also exemplified CUBIC-cancer analysis with a Panc-1 cell liver metastasis model (Figure S3C). This highly reproducible analysis would overcome enduring issues in our understanding of *in vivo* metastatic progression in various cancers. Thus, CUBIC-cancer analysis enabled the complete quantification of metastatic colonies in an individual tumor-bearing mouse.

To verify CUBIC-cancer analysis as a general purpose platform, several lung metastasis models derived from various types of cancer cells were examined (Figure 3C). The detected red-color signals were shown to have originated from mCherry, using immunohistochemical staining with anti-mCherry antibody (Figures 3D and S3D). In the experimental metastasis models, all mouse cancer cells, i.e., 4T1, B16F10, and Renca cells, tended to grow to large colonies, while the morphologies of these colonies were all different. In case of experimental metastasis

(C) Whole-body imaging of the experimental peritoneal dissemination model by intraperitoneal injection with SUIT-2 cells in BALB/c-*nu/nu* mice. WBI and abdominal organ images in liver (L) and intestine (I) (leftmost and second from left) and magnified 3D and XY images (third from left and rightmost) are shown (SUIT-2, GFP; nuclei, PI).

(D) Quantification of the cell number and the volume of metastatic colonies. Spot analysis and surface analysis were applied to the magnified images in (C).

(E) Whole-body imaging of the spontaneous metastasis model with orthotopic injection of Renca cells in BALB/c mice. WBI and organ images in lung (Lu), heart (H), liver (L), kidney (K), pancreas (P), and lymph nodes (LN) (leftmost and second from left) and magnified 3D and XY images (third from left and rightmost) are shown (Renca, mCherry; nuclei, RedDot2).

(F) Quantification of the cell number and the volume of metastatic colonies. Spot analysis and surface analysis were applied to the magnified images in (E). See also Figure S2 and Table S1.

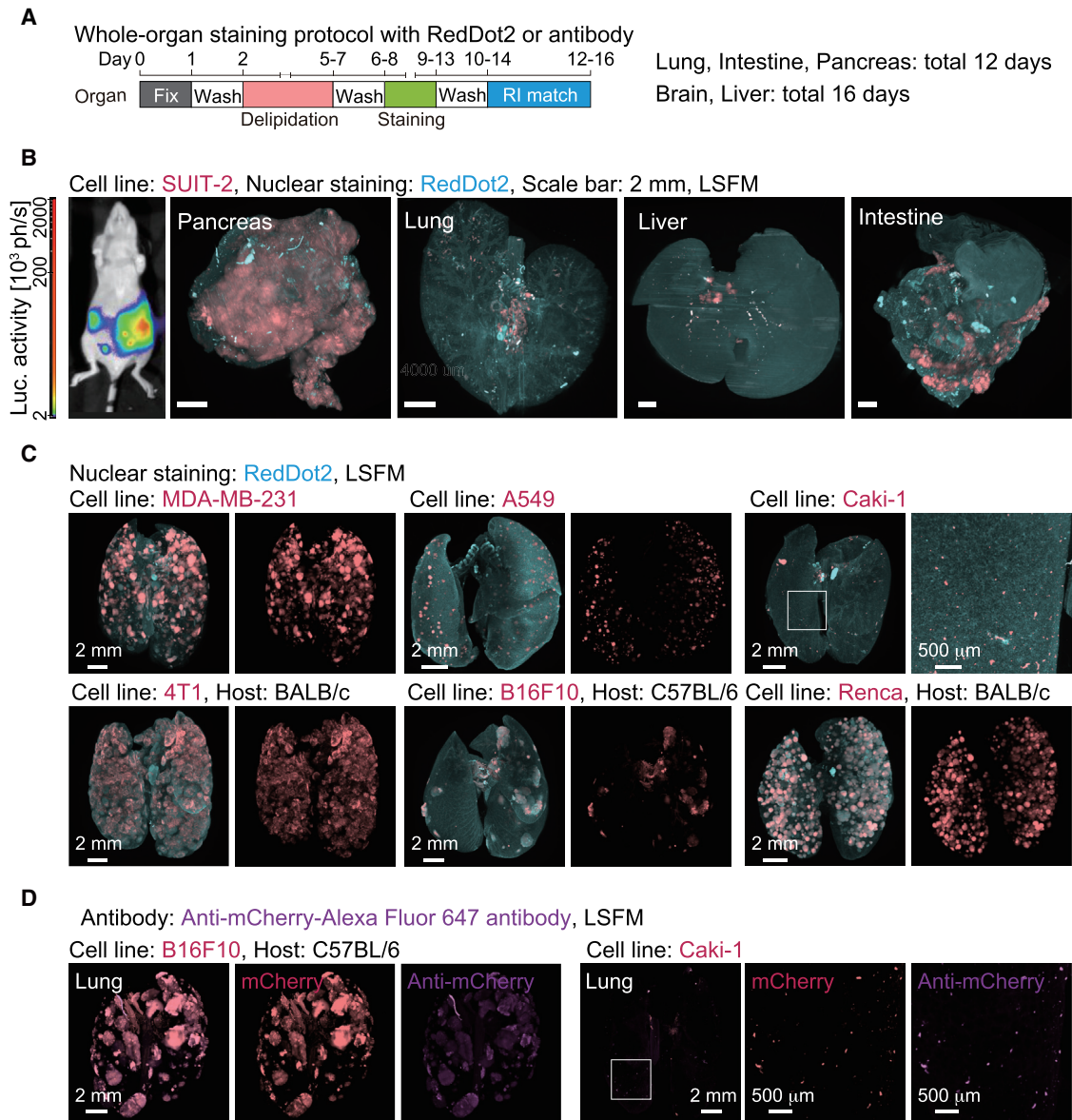


Figure 3. Whole-Organ Imaging of Various Cancer Metastasis Models

(A) Whole-organ staining protocols with RedDot2 or antibody.

(B) Whole-organ imaging of the spontaneous metastasis model with orthotopic injection of SUIT-2 cells in BALB/c-*nu/nu* mice. The bioluminescence image (leftmost) and primary tumors in the pancreas and the metastatic colonization in the distant organs (second, third, and fourth from left and rightmost) are shown (SUIT-2, mCherry; nuclei, RedDot2).

(C) Whole-lung imaging of several metastasis models. In the experimental lung metastasis model, cancer cells (MDA-MB-231, A549, 4T1, B16F10, and Renca) were intravenously injected in mice. In case of spontaneous metastasis, Caki-1 cells were orthotopically injected into the kidney (cancer cell, mCherry; nuclei, RedDot2).

(D) Whole-lung 3D immunohistochemistry with anti-mCherry antibody (cancer cell, mCherry; anti-mCherry, Alexa Fluor 647). White insets were magnified next to the whole-lung images in (C) and (D).

See also [Figure S3](#).

with human cancer cells, MDA-MB-231 cells also formed large colonies throughout the lungs compared to A549 cells. In contrast, in spontaneous lung metastasis with Caki-1 cells, metastatic colonies were observed throughout the lungs, but their volumes were small. Overall, we succeeded in applying

CUBIC-cancer analysis to 13 different mouse models with nine cancer cell lines ([Table S1](#)).

These results demonstrate that whole-organ CUBIC-cancer analysis is a systematic, robust, widely applicable, and immunolabeling-compatible analytical platform for cancer metastasis.

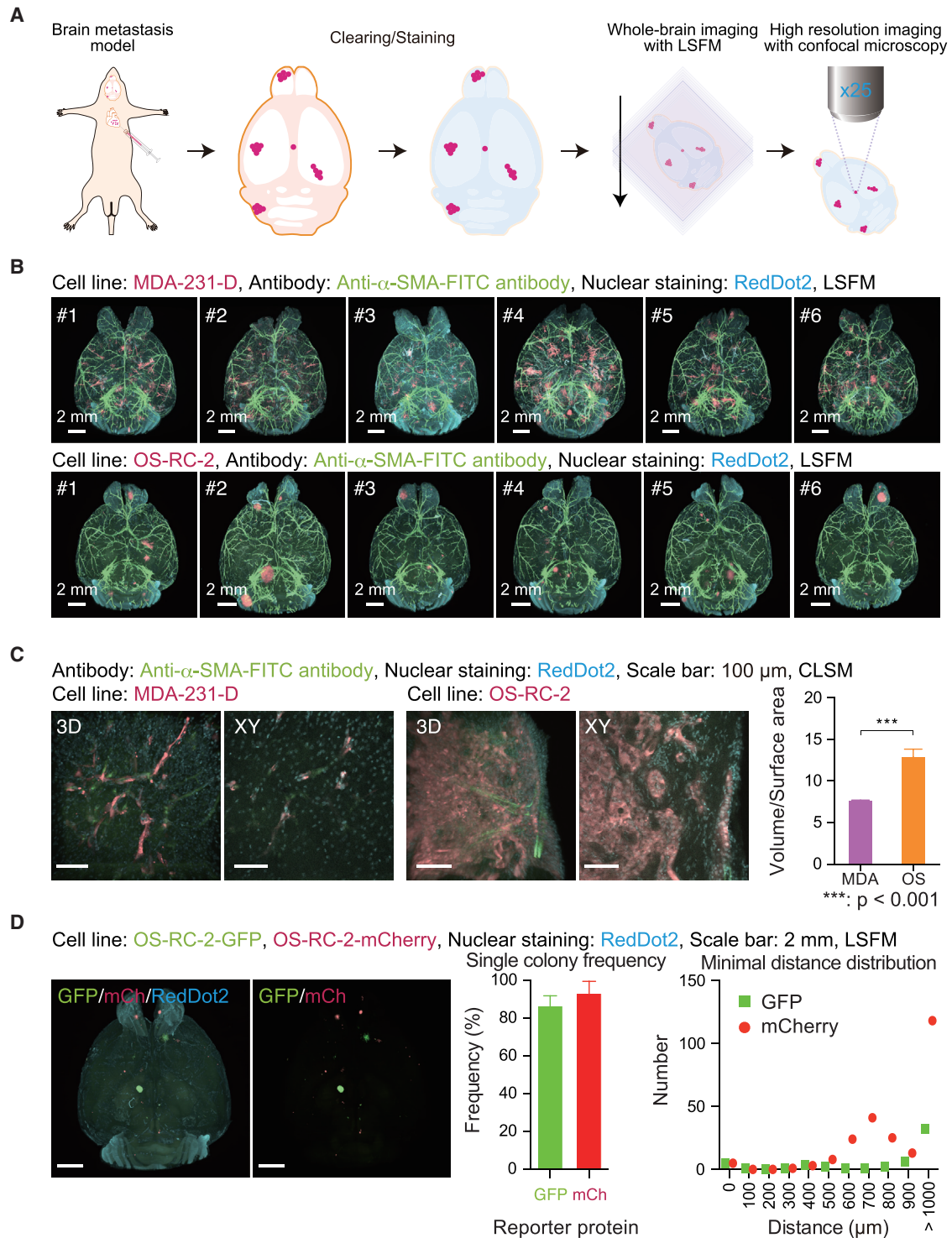


Figure 4. 3D Analysis of the Metastatic Patterns in Experimental Brain Metastasis Models

(A) Scheme of the experimental procedure.

(B) Whole-brain imaging of the experimental brain metastasis models with MDA-231-D cells or OS-RC-2 cells in BALB/c-*nu/nu* mice. The 3D images of the brain samples are shown (upper, MDA-231-D at day 28; lower, OS-RC-2 at day 40; cancer cell, mCherry; α -SMA, FITC; nuclei, RedDot2). Animal number of each group is $n = 6$.

(legend continued on next page)

CUBIC-Cancer Analysis Enables Monitoring of the Different Patterns of Brain Metastasis Formation with Blood Vessels in 3D

Brain metastasis is frequently observed in melanoma and some other cancers, and it results in a high risk of mortality (Gavrilovic and Posner, 2005; Nussbaum et al., 1996). Recently, two-photon microscopy-based analytical methods have clarified the correlation between brain metastasis and the cerebral blood vasculature (Carbonell et al., 2009; Kienast et al., 2010). Nevertheless, quantitative and statistical analyses of the spatial distribution of all metastatic colonies throughout the brain are still challenging. Thus, we investigated whether our CUBIC-cancer analysis can be used to classify the potentially different types of brain metastasis by quantitatively and statistically analyzing metastatic colonies in the entire organ (Figure 4A). The brain metastasis model of MDA-231-D cells was compared with another model using OS-RC-2 cells. Although there appeared to be no distinct difference in metastatic features between these models by *in vivo* bioluminescence imaging (Figure S4A), CUBIC-cancer analysis clearly showed that metastatic colonies in these models exhibited different histological patterns (Figure 4B).

Many colonies of MDA-231-D cells were localized with α -SMA-positive vascular smooth muscle cells. On the other hand, most colonies of OS-RC-2 cells were distant from α -SMA-positive vascular smooth muscle cells (Figure 4B). In addition, these metastatic morphological features were also identified by the histological analysis based on HE staining with or without CUBIC-cancer analysis (Figure S4B). To quantify the morphological features, we used the index “volume per surface area,” which was positively correlated with the roundness of the colony, and we found a significant difference between the two metastatic models (Figure 4C). Furthermore, the colonies of MDA-231-D cells tended to be smaller and closer to the blood vessels than those of OS-RC-2 cells (Figure S4C). These results suggest that the colony formation of OS-RC-2 cells in the brain may be dependent on cancer cell-mediated neovascularization (angiogenic growth), whereas MDA-231-D cells may be able to migrate toward pre-existing vasculatures and hijack them during the process of metastasis (co-optive growth).

For elucidating the mechanism of cancer metastasis, it is important to determine whether brain metastatic foci are generated by a single cell. To test this, equal numbers of mCherry- or GFP-expressing OS-RC-2 cells were mixed and used for intracardiac injection into the same mouse. CUBIC-cancer analysis revealed that most mCherry-positive cells in the brain were separate from the colonies of GFP-positive cells (Figure 4D), thus revealing the metastatic properties of individual cancer cells.

CUBIC-Cancer Analysis Is Applicable to Statistical Spatiotemporal Analysis during the Initial Steps of Metastatic Progression

The statistical spatiotemporal analysis of cancer metastasis in an entire organ has the potential to be a powerful tool for cancer research. To visualize time-dependent cancer metastasis, an experimental lung metastasis model with MDA-231-D cells was used in combination with CUBIC-cancer analysis. We then carried out whole-lung imaging of metastatic foci or colonies (Figure 5A). To ensure the non-biased exhaustive detection of size-variable metastatic foci, the average volume of nuclei was adopted as the threshold for focus detection (Figure S5A). Immunodeficient BALB/*c-nu/nu* mice and immunocompetent BALB/*c* mice were intravenously injected with MDA-231-D cells, and metastatic foci were detected by CUBIC-cancer analysis 1 hr after injection (Figures 5B and 5C). In total, three to four mice at each time point were analyzed (Figures S5B and S5C).

In BALB/*c-nu/nu* mice, numerous metastatic foci spread throughout the lung were drastically eliminated within 1 day after injection (Figure 5D). Although the number of foci continued to decrease after day 1, the average volume of the foci markedly increased from day 3, suggesting metastatic colonization. On the other hand, in BALB/*c* mice, metastatic foci were thoroughly excluded without any colonization (Figures 5E and S5C). Confocal images were used to quantify the emerged metastatic colonies on day 14 in BALB/*c-nu/nu* mice and the accumulated cell aggregations in BALB/*c* mice on day 3 (Figures 5F and 5G). Since the mCherry signals were often surrounded by those of the cell aggregations, the aggregations likely reflected the immune response of the host (Figure 5H). Overall, CUBIC-cancer analysis enabled not only a statistical time course analysis of cancer metastasis but also direct observations of the stochastic immune-mediated elimination of metastatic foci.

CUBIC-Cancer Analysis Reveals that the Epithelial-Mesenchymal Transition Might Promote Not Only the Extravasation but Also the Survival of Cancer Cells at Metastatic Sites

The epithelial-mesenchymal transition (EMT) is known to play a pivotal role in cancer metastasis. Although roles of EMT in the intravasation of cancer cells have been demonstrated (Nieto et al., 2016; Tsai and Yang, 2013), it has not been clearly determined whether the EMT is involved in the extravasation of cancer cells (Nieto et al., 2016; Tsai and Yang, 2013). Thus, we aimed to elucidate the EMT involvement in the extravasation of cancer metastasis *in vivo* by CUBIC-cancer analysis. In accordance with a previous report (Saito et al., 2009), induction of the EMT in A549 cells by TGF- β stimulation was confirmed by gene profiling and morphological examination (Figures S6A and S6B).

(C) Quantification of the morphological features in the two metastatic models. Magnified 3D and XY images of typical metastatic foci are shown. Surface analysis was applied to the 3D images in (B). As a characteristic indicator of different metastatic patterns, the volume of the foci divided by its surface area was calculated. Data represent mean \pm SEM (***) $p < 0.001$.

(D) Lineage analysis using renal cancer cell lines expressing GFP or mCherry. The 3D images of the brains stained with RedDot2 (left), the frequency of the metastatic colonies consisting of a single color (middle), and the minimal distance mean \pm SD between metastatic colonies expressing GFP or mCherry (right) are shown. Data represent mean \pm SD.

See also Figure S4.

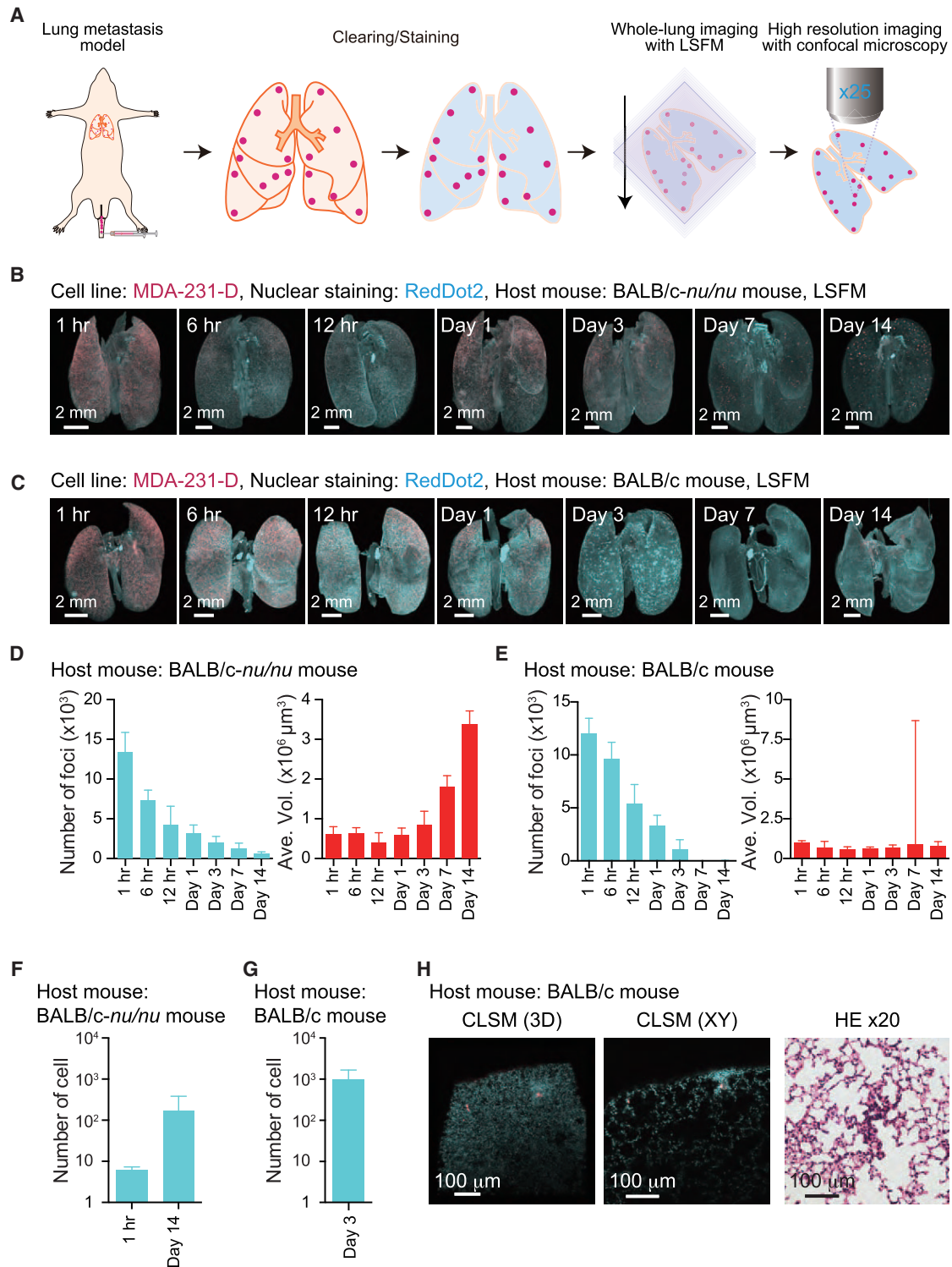


Figure 5. Spatiotemporal Dynamics of Metastatic Progression in the Experimental Lung Metastasis Model

(A) Scheme of the experimental procedure.

(B and C) Time course images of the experimental lung metastasis model with MDA-231-D cells in BALB/c-*nu/nu* mice (B) or BALB/c mice (C). BALB/c-*nu/nu* mice or BALB/c mice were intravenously injected with MDA-231-D cells. The 3D images of the lung samples at the indicated time points are shown (MDA-231-D, mCherry; nuclei, RedDot2).

(legend continued on next page)

To investigate the EMT roles in cancer cell arrest in microvessels of distant organs and extravasation, BALB/c-*nu/nu* mice were intravenously injected with A549 cells pre-treated with or without TGF- β (Figure 6A). Metastatic foci of A549 cells were clearly detected throughout the lung, and the colonization of the metastatic foci gradually progressed over 14 days after the early intensive elimination (Figure 6B). Confocal images allowed the visualization of metastatic foci around alveoli 1 hr after injection, and they showed the appearance of spheres regardless of TGF- β stimulation 14 days after injection. Interestingly, statistical analysis revealed that TGF- β stimulation significantly increased the number of metastatic foci from 1 to 14 days (Figure 6C).

In addition, the histological investigation after CUBIC-cancer analysis revealed that there was no clear difference between unstimulated and TGF- β -pre-stimulated cancer cells in the expression of E-cadherin in metastatic colonies 14 days after injection (Figure 6D). CUBIC-cancer analysis may thus be of value in elucidating unresolved issues regarding the *in vivo* role of the EMT in tumor metastasis.

CUBIC-Cancer Analysis Enables the Pharmacotherapeutic Profiling of Anti-tumor Drugs against Cancer Metastasis

Finally, we attempted to establish a therapeutic evaluation system for metastatic whole-lung cancers by statistically profiling metastatic cells. To assess chemotherapeutic responses in a syngeneic mouse tumor model, wild-type BALB/c mice were injected with 4T1 cells intravenously and treated with the anti-tumor drugs doxorubicin (Dox), 5-FU, and cyclophosphamide (CPA) (Figure 7A). Eight days after 4T1 injection, the proliferation of metastatic colonies tended to be suppressed in the drug-treated groups (Figures 7B and 7C). In particular, CPA significantly reduced both the total volume and number of colonies. The daily administration of 5-FU resulted in the drastic reduction of metastatic colonies (Figure 7D). Importantly, many metastatic foci were still detected in the lungs of 5-FU-treated mice, indicating the high sensitivity of CUBIC-cancer analysis. Some foci were composed of just a single cancer cell, which might be dormant or resistant to anti-tumor drugs (Figures 7D and 7E). Taken together, CUBIC-cancer analysis can be used to evaluate the *in vivo* effects of anti-tumor drugs at the single-cell level.

DISCUSSION

RI-Optimized CUBIC Protocol Enables the Scalable Whole-Body Cell Profiling of Various Cancer Models

The RI values of tissue and cell structures are highly diverse, ranging from 1.34 to 1.59, because the RI for each intact biological tissue depends on the contents and densities of lipids, pro-

teins, and other constituents (Tuchin, 2015). Therefore, optimal RI values were likely to be dependent on each organ. The results of the transmittance evaluation of major organs mounted on various RI media indicated that the transparency of the organs tended to increase as the RI values increased (Figures 1C and S1B). Interestingly, this tendency was observed regardless of the organ, suggesting that these organs mostly contain the constituents with relatively similar RI values. We noted that the RI value-dependent increase in the transparency of most of the organs did not reach a plateau, even at an RI of 1.52. It would be very difficult to prepare hydrophilic RI-matching media with higher RI values (RI > 1.52) using current chemical candidates, because of their water solubility or low RI value per unit mass. Future development of such RI-matching media (RI > 1.52) may be favorable to make these organs transparent more efficiently. Another technical challenge is to develop whole-body-clearing protocols compatible with bone tissue clearing. Mild, effective, and highly permeable decalcification methods compatible with our CUBIC protocol would facilitate our understanding of the mechanisms of cancer metastases, including bone metastasis. We noted that perfusion-assisted agent release *in situ* (PARS) and ultimate 3D imaging of solvent-cleared organs (uDISCO) protocols might be also applicable to whole-body profiling of cancer metastasis with a single-cell resolution (Pan et al., 2016; Susaki et al., 2015; Tanaka et al., 2014; Yang et al., 2014). Therefore, comparison of the characteristics of the proposed CUBIC-cancer protocol in this study with those of these two methods would be important in the future.

CUBIC-Cancer Analysis Provides a Global Analytical Pipeline of Cancer Metastasis by Bridging the Resolution Gap between Conventional *In Vivo* Bioluminescence Imaging and 2D Histology

To obtain an overview of cancer metastasis, it would be important to create a global analytical pipeline visualizing the overall dynamics of metastatic progression, spatiotemporal distribution of metastatic colonies at single-cell resolution, and their surrounding microenvironments. In this study, we attempted to bridge the resolution gap between *in vivo* bioluminescence imaging and 2D histology by our scalable CUBIC-cancer analysis, using cancer cell lines stably expressing luciferase and fluorescent proteins.

We determined whether fluorescent signals in whole-body and whole-organ images actually originated from cancer cells or indirectly originated from some other cells, such as phagocytes that digested labeled cancer cells. To compare the *in vivo* bioluminescence imaging and CUBIC-cancer analysis, we performed *in vivo* bioluminescence imaging before tissue clearing.

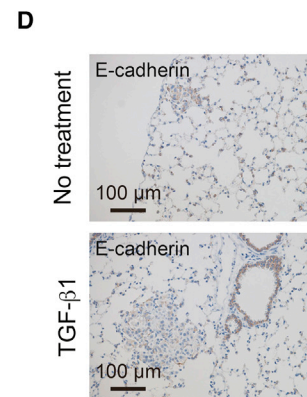
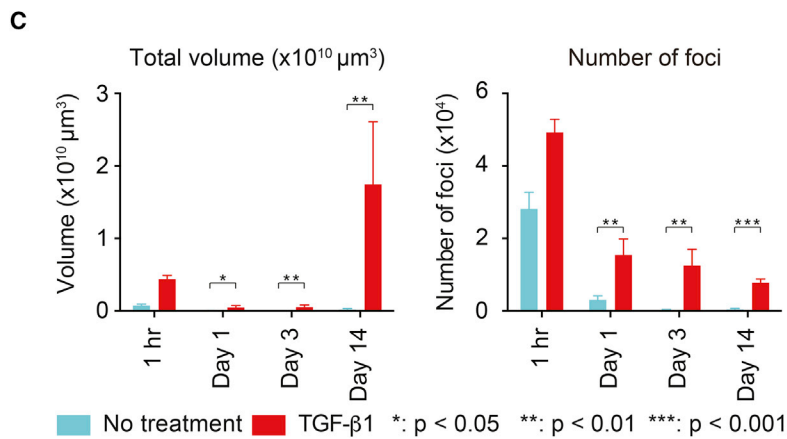
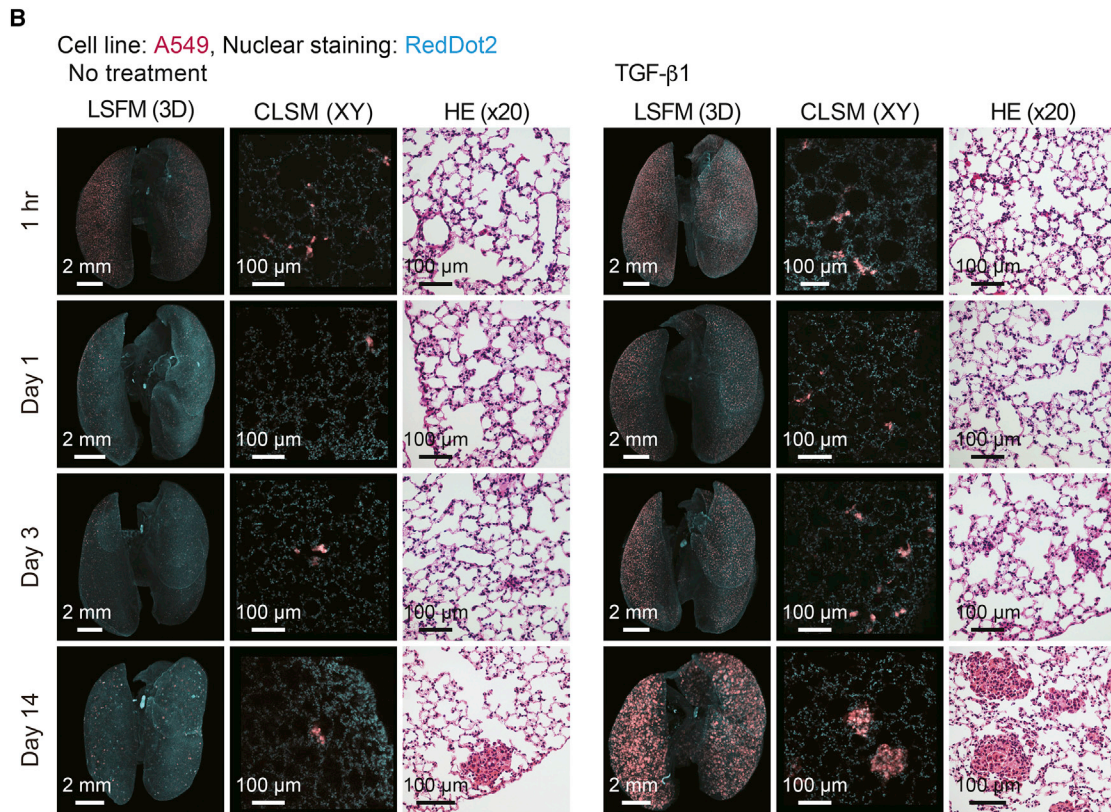
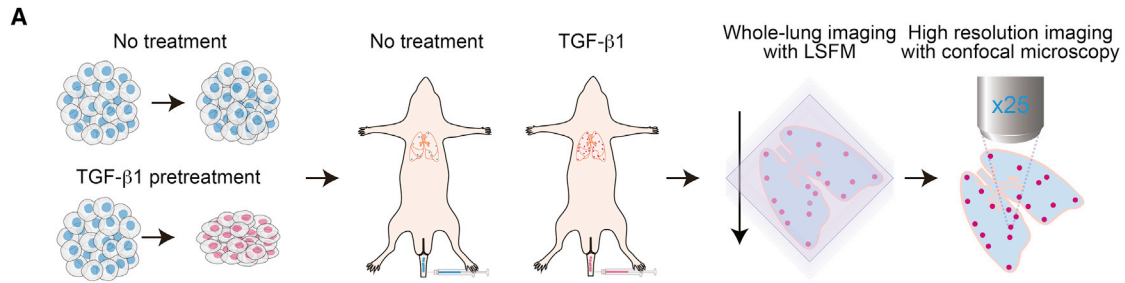
(D and E) Quantification of the metastatic foci in BALB/c-*nu/nu* mice (D) or BALB/c mice (E). The number and the average volume of foci from (B) or (C) are shown. Animal number at each time point is $n = 3-4$. Data represent mean \pm SD.

(F) Quantification of the cell number of metastatic colonies. Spot analysis and surface analysis were applied to the 3D images in (B). Data represent mean \pm SD.

(G) Quantification of the cell number of cell aggregates observed in BALB/c mice. Spot analysis and surface analysis were applied to the 3D images of day 3 in (C). Data represent mean \pm SD.

(H) Representative magnified 3D and XY images of the lungs containing the cell aggregates at day 3 after injection in BALB/c mice (left and middle) (MDA-231-D, mCherry; nuclei, RedDot2). The typical HE staining pattern after CUBIC-cancer analysis including the cell aggregates (right most) is shown.

See also Figure S5.



(legend on next page)

Bioluminescence images from luciferase activity roughly corresponded to the fluorescent signals (Figures 2B, 3B, S2C, and S3C), despite apparent differences in multiple organ metastases by Renca cells (Figures 2E and S2A) and brain metastasis by MDA-231-D cells (Figures 4B and S4A). In the former case, bioluminescence signals in metastatic organs may not have been detected with this dynamic range because the signals were too intense at the primary lesion. In the latter case, bioluminescence signals may have been shielded by the skull, and they seemed to leak out to the eyes and neck (Figure S4A). In addition, because we could perform HE staining of CUBIC-treated organs, we compared the CUBIC-cancer analysis results with the data obtained by the conventional histological method. We found that the basic tissue pathology was well preserved in HE staining, and we could detect the tumors in the CUBIC-treated samples (Figures 2B and 6B). However, the histology of the metastatic tumors of OS-RC-2 cells, which are clear cell renal carcinoma and contain high amounts of glycogen, was distinct between the intact samples and samples after CUBIC-cancer analysis, possibly because of the delipidation process (Figure S4B). These observations indicated that certain CUBIC-treated samples can be used for immunohistochemical analysis, although the cell membrane in the samples may be damaged due to delipidation. Together, CUBIC-cancer analysis could successfully bridge the resolution gap between conventional *in vivo* bioluminescence imaging and 2D histology.

EMT Significantly Promotes the Extravasation or Survival of Cancer Cells *In Vivo*

The EMT contributes to the metastatic process of intravasation in cancer metastasis (Nieto et al., 2016; Polyak and Weinberg, 2009). Cancer cells that have undergone EMT participate in extravasation by enhancing the attachment of cancer cells to metastatic sites through the induction of matrix metalloproteinases or formation of filopodia-like protrusions (Labelle et al., 2011; Shibue et al., 2012). In this study, we investigated the relevance of the EMT in lung metastasis by statistical and temporal analysis of metastatic colonies in an experimental extravasation model (Figure 6). The nature of the *in vivo* dynamics of metastatic extravasation is an ongoing controversy. While the metastatic extravasation was postulated to proceed over 1–2 days (Tsai and Yang, 2013), another group demonstrated using an *in vitro* extravasation assay that cancer cells could extravasate from microvessels within 3 hr (Spiegel et al., 2016). Our results showed that the number of foci at 1 hr after injection was not significantly different, suggesting that the EMT appears to be not involved in the arrest of cells in microvessels. To our surprise,

the number of metastatic foci markedly increased on day 1 after the injection of cells pre-treated with TGF- β 1, and this number was approximately sustained up to day 14 (Figure 6C). These findings suggest that the fate of cancer cells in metastatic sites is determined in the very early phase (within a day) after arriving at distant organs, and that the EMT might be associated with the survival of cancer cells at metastatic sites. The EMT is thought to confer stem cell-like features that allow cells to disseminate and gain resistance to apoptosis or anti-tumor therapies (Polyak and Weinberg, 2009). Hence, the significant promotion of metastasis by EMT induction may reflect the transformation of differentiated cells into a stem cell-like phenotype, including the induction of extracellular matrix production and gaining of the resistance to apoptosis.

Plasticity between the epithelial and mesenchymal phenotypes also plays a pivotal role in the process of metastasis (Ye and Weinberg, 2015). In clinical studies, intravasated cancer cells circulating in the blood have been shown to exhibit the mesenchymal phenotype, while colonized cancer cells in organs were found to exhibit the epithelial phenotype (Kallergi et al., 2011; Kowalski et al., 2003). Because of the relatively short-term stimulation of A549 cells by TGF- β 1 in the present study, we assumed that the plasticity of the EMT was maintained in this experiment. In fact, our results suggested that A549 cells that colonized the lung were restored to the epithelial phenotype with the restoration of E-cadherin expression. Taken together, our CUBIC-cancer analysis clarified the *in vivo* dynamics of the plasticity between the epithelial and mesenchymal phenotypes during the progression of cancer metastasis through the statistical analysis of metastatic foci at the whole-organ level.

CUBIC-Cancer Analysis Provides an *In Vivo* Therapeutic Evaluation System to Aid in the Treatment of Metastatic Tumors

To quantitatively evaluate the therapeutic effects of anti-tumor drugs, it is necessary to establish an ultra-sensitive detection system that can determine whether metastatic colonies are completely eliminated or whether single cancer cells resistant to anti-tumor drugs still remain. This distinction is particularly important because the emergence of chemoresistant cancer cells eventually leads to the proliferation of cancer cells and the development of incurable tumors. It is difficult to detect metastasized cells at single-cell resolution by *in vivo* bioluminescence imaging, and visualizing whole-organ images by 2D histology is labor intensive. Notably, our CUBIC-cancer analysis of the entire lung successfully detected tiny foci consisting of even a single cancer cell (Figures 7D and 7E). Therefore, our

Figure 6. *In Vivo* Role of the EMT Induced by TGF- β Pre-treatment in the Progression of Lung Metastasis

(A) Scheme of the experimental procedure.

(B) Time course images of the experimental lung metastasis model with A549 cells. A549 cells pre-treated without (left) or with (right) TGF- β 1 were intravenously injected in BALB/c-*nu/nu* mice. The 3D images of the lung samples at the indicated time points are shown (A549, mCherry; nuclei, RedDot2). Representative images of HE staining after CUBIC-cancer analysis are also shown.

(C) Quantification of the volume and the number of foci of metastatic colonies pre-treated with or without TGF- β 1. Surface analysis was applied to the 3D images in (B). Animal number at each time point is $n = 4$. Data represent mean \pm SD.

(D) Immunohistochemistry of E-cadherin. Samples on day 14 after CUBIC-cancer analysis were subjected to immunohistochemistry with anti-E-cadherin antibody.

See also Figure S6.

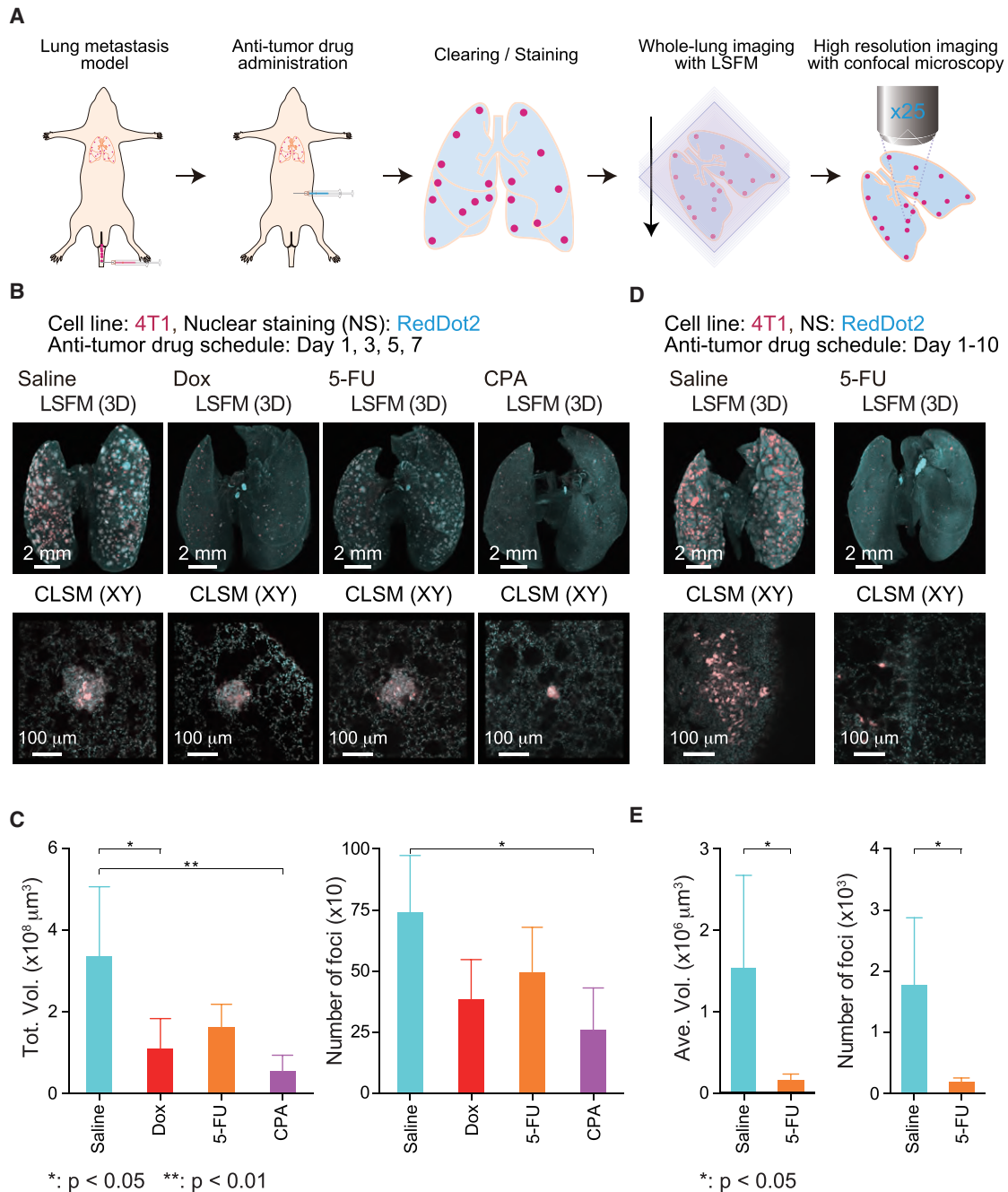


Figure 7. Quantitative Evaluation of Therapeutic Effects of Anti-tumor Drugs in an Experimental Lung Metastatic Model

(A) Scheme of the experimental procedure.

(B) In vivo therapeutic efficacy of anti-tumor drugs. The 3D images of the lung samples are shown (4T1, mCherry; nuclei, RedDot2).

(C) Quantification of pharmacotherapeutic effects of anti-tumor drugs. Animal number of each group is $n = 4$. Data represent mean \pm SD.

(D) In vivo therapeutic evaluation of once daily treatment with 5-FU. The 3D images of the lung samples are shown (4T1, mCherry; nuclei, RedDot2).

(E) Quantification of pharmacotherapeutic effect of once daily treatment with 5-FU. Animal number of each group is $n = 4$ (5-FU) and $n = 5$ (saline). Data represent mean \pm SD.

CUBIC-cancer analysis may provide critical information for the development of a curative treatment for metastasis.

Furthermore, we wish to emphasize another important advantage of CUBIC-cancer analysis: it allows a seamless connection

between in vivo live imaging and 2D histology, complementing the shortcomings of each modality. The global analytical pipeline consisting of these methods is quite robust and reliable, because the experimental data could be thoroughly verified

by the three modalities. An *in vivo* therapeutic evaluation system is urgently needed not only for malignant neoplastic diseases but also for autoimmune diseases, which remain a challenge clinically, and emerging induced pluripotent stem cell (iPSC)-based regenerative therapies. This analytical pipeline would have great potential for becoming a *de facto* standard for an *in vivo* therapeutic evaluation system for complex systemic diseases.

EXPERIMENTAL PROCEDURES

Details are also supplied in the [Supplemental Experimental Procedures](#).

Preparation of Clearing Solutions

Clearing solutions were composed of four chemicals, which were selected from chemical screening (T.C. Murakami and K. Tainaka, unpublished data). CUBIC-L for decolorization and delipidation was prepared as a mixture of 10 w% polyethylene glycol mono-*p*-isooctylphenyl ether/Triton X-100 (12967-45, Nacalai Tesque) and 10 w% *N*-butyl-diethanolamine (B0725, Tokyo Chemical Industry). CUBIC-R for RI matching was prepared as a mixture of 45 w% 2,3-dimethyl-1-phenyl-5-pyrazolone/antipyrine (D1876, Tokyo Chemical Industry) and 30 w% nicotinamide (N0078, Tokyo Chemical Industry) ([Table S2](#)). See also the [Supplemental Experimental Procedures](#).

Microscopy

Whole-body and whole-organ images were acquired with a custom-build LSM (developed by Olympus). High-resolution images for cell profiling were acquired with CLSM (FLUOVIEW FV1200, Olympus). The RI-matched sample was immersed in a mixture of silicon oil HIVAC-F4 (Shin-Etsu Chemical) and mineral oil (RI = 1.467, M8410, Sigma-Aldrich) during image acquisition. See also the [Supplemental Experimental Procedures](#).

Experimental and Spontaneous Mouse Metastatic Tumor Models

Inbred wild-type BALB/c mice, C57BL/6 mice, and BALB/*c-nu/nu* mice were purchased from Sankyo Labo Service. All experiments were approved and carried out according to the Animal Care and Use Committee of the Graduate School of Medicine, The University of Tokyo. Each metastasis model is described briefly. For experimental liver metastasis, BALB/*c-nu/nu* mice (5 weeks old, female) were injected with Panc-1 cells by open injection in the spleen. For peritoneal dissemination, SUIT-2 cells were injected into pancreas orthotopically or intraperitoneally in BALB/*c-nu/nu* mice (5 weeks old female). For experimental lung metastasis by intravenous injection, BALB/*c-nu/nu* (5 weeks old, female), BALB/c mice (5 weeks old, female or male), or C57BL/6 mice (5 weeks old, female) were injected with each cell line (MDA-MB-231, MDA-231-D, A549, 4T1, Renca, and B16F10 cells). For spontaneous lung metastasis by renal subcapsule injection, BALB/c (5 weeks old, male) or BALB/*c-nu/nu* (5 weeks old, male) mice were injected with Renca, OS-RC-2, or Caki-1 cells orthotopically. For experimental brain metastasis by intracardiac injection, BALB/*c-nu/nu* (4 weeks old, female MDA-231-D, male OS-RC-2) mice were injected with MDA-231-D or OS-RC-2 cells by puncture into the left ventricle of heart. For the stimulation with TGF- β , A549 cells were pre-treated with or without TGF- β 1 (5 ng/mL) for 72 hr in culture and subjected to *in vivo* experiment. See also the [Supplemental Experimental Procedures](#).

Statistical Analysis

An unpaired *t* test was used to compare the index of volume per surface area of brain metastasis and to compare the pharmacotherapeutic effects of 5-FU for statistical significance. Multiple *t* tests were used to compare the effect of TGF- β 1 stimulation for statistical significance. Dunnett's multiple comparisons test was used to examine the pharmacotherapeutic effects of anti-tumor drugs for statistical significance. All statistical analyses were performed with GraphPad Prism6 software.

SUPPLEMENTAL INFORMATION

Supplemental Information includes Supplemental Experimental Procedures, six figures, and four tables and can be found with this article online at <http://dx.doi.org/10.1016/j.celrep.2017.06.010>.

AUTHOR CONTRIBUTIONS

H.R.U., K.M., S.I.K., K. Takahashi, K. Tainaka, and S.E. designed the study. S.I.K. performed most of the imaging and analysis of metastasis model mice. K. Takahashi and J.N. performed most of the establishment of cancer cell lines for CUBIC-cancer analyses and preparation of metastasis model mice. Y.M. contributed to the histological experiments. H.R.U., K.M., S.I.K., K. Takahashi, K. Tainaka, and S.E. wrote the manuscript. All authors discussed the results and commented on the manuscript text.

ACKNOWLEDGMENTS

We thank all lab members at The University of Tokyo and RIKEN QBiC, in particular, A. Millius for editing, T.C. Murakami and C. Shimizu for chemical screening for tissue clearing, S. Kitamura and K. Nakamura for developing optimized delipidation medium, M. Fujiwara for developing RI-optimized medium, E.A. Susaki and A. Kuno for developing 3D staining methods, S. Shoi for helping with statistical analysis, R. Ohno for housing mice, and Bitplane for instruction on Imaris 8.1.2. We also thank Y. Katsuno and F. Murai for plasmid preparation and H. Miyoshi (RIKEN) for providing the lentiviral vectors. This work was supported by grants from AMED-CREST (Japan Agency for Medical Research and Development [AMED]/Ministry of Education, Culture, Sports, Science and Technology, Japan [MEXT], H.R.U.); CREST (JST/MEXT, H.R.U.); Brain/MINDS (AMED/MEXT, H.R.U.); Basic Science and Platform Technology Program for Innovative Biological Medicine (AMED/MEXT, H.R.U.); Grants-in-Aid for Scientific Research from the Japan Society for the Promotion of Science (JSPS) (KAKENHI grant 14J01180 to S.I.K., grant 17J30007 to S.I.K., grant 13J10991 to K. Takahashi, and grant 16J05993 to J.N.), Grant-in-Aid for Challenging Exploratory Research (JSPS KAKENHI grant 16K15124 to K. Tainaka), Grants-in-Aid for Scientific Research (S) (JSPS KAKENHI grants 25221004 to H.R.U. and 15H05774 to K.M.), and Grants-in-Aid for Scientific Research on Innovative Areas (JSPS KAKENHI grant 23115006 to H.R.U.); and Brain Protein Aging and Dementia Control (17H05688 to K. Tainaka) from MEXT; a grant for Practical Research for Innovative Cancer Control (16ck0106193h0001) from AMED (K.M.); and a Specific Research Grant from The Tokyo Society of Medical Sciences (S.E.). T.C. Murakami, K. Tainaka, and H.R.U. have filed a patent application for CUBIC-reagents. A part of this study was done in collaboration with the Olympus Corporation.

Received: March 24, 2017

Revised: May 2, 2017

Accepted: May 29, 2017

Published: July 5, 2017

REFERENCES

- Carbonell, W.S., Ansoorge, O., Sibson, N., and Muschel, R. (2009). The vascular basement membrane as "soil" in brain metastasis. *PLoS ONE* 4, e5857.
- Chung, K., Wallace, J., Kim, S.Y., Kalyanasundaram, S., Andalman, A.S., Davidson, T.J., Mirzabekov, J.J., Zalocusky, K.A., Mattis, J., Denisin, A.K., et al. (2013). Structural and molecular interrogation of intact biological systems. *Nature* 497, 332–337.
- Cuccarese, M.F., Dubach, J.M., Pfirsche, C., Engblom, C., Garris, C., Miller, M.A., Pittet, M.J., and Weissleder, R. (2017). Heterogeneity of macrophage infiltration and therapeutic response in lung carcinoma revealed by 3D organ imaging. *Nat. Commun.* 8, 14293.
- Dotd, H.U., Leischner, U., Schierloh, A., Jährling, N., Mauch, C.P., Deininger, K., Deussing, J.M., Eder, M., Ziegglänsberger, W., and Becker, K. (2007).

- Ultramicroscopy: three-dimensional visualization of neuronal networks in the whole mouse brain. *Nat. Methods* 4, 331–336.
- Ertürk, A., Becker, K., Jährling, N., Mauch, C.P., Hojer, C.D., Egen, J.G., Hellal, F., Bradke, F., Sheng, M., and Dodt, H.U. (2012). Three-dimensional imaging of solvent-cleared organs using 3DISCO. *Nat. Protoc.* 7, 1983–1995.
- Gavrilovic, I.T., and Posner, J.B. (2005). Brain metastases: epidemiology and pathophysiology. *J. Neurooncol.* 75, 5–14.
- Hama, H., Kurokawa, H., Kawano, H., Ando, R., Shimogori, T., Noda, H., Fukami, K., Sakae-Sawano, A., and Miyawaki, A. (2011). Scale: a chemical approach for fluorescence imaging and reconstruction of transparent mouse brain. *Nat. Neurosci.* 14, 1481–1488.
- Johnsen, S., and Widder, E.A. (1999). The physical basis of transparency in biological tissue: ultrastructure and the minimization of light scattering. *J. Theor. Biol.* 199, 181–198.
- Kallergi, G., Papadaki, M.A., Politaki, E., Mavroudis, D., Georgoulas, V., and Agelaki, S. (2011). Epithelial to mesenchymal transition markers expressed in circulating tumour cells of early and metastatic breast cancer patients. *Breast Cancer Res.* 13, R59.
- Ke, M.T., Fujimoto, S., and Imai, T. (2013). SeeDB: a simple and morphology-preserving optical clearing agent for neuronal circuit reconstruction. *Nat. Neurosci.* 16, 1154–1161.
- Kienast, Y., von Baumgarten, L., Fuhrmann, M., Klinkert, W.E., Goldbrunner, R., Herms, J., and Winkler, F. (2010). Real-time imaging reveals the single steps of brain metastasis formation. *Nat. Med.* 16, 116–122.
- Kowalski, P.J., Rubin, M.A., and Kleer, C.G. (2003). E-cadherin expression in primary carcinomas of the breast and its distant metastases. *Breast Cancer Res.* 5, R217–R222.
- Labelle, M., Begum, S., and Hynes, R.O. (2011). Direct signaling between platelets and cancer cells induces an epithelial-mesenchymal-like transition and promotes metastasis. *Cancer Cell* 20, 576–590.
- Nicholls, A.G. (1927). The fourth chapter in the history of pathology. *Can. Med. Assoc. J.* 17, 843–845.
- Nieto, M.A., Huang, R.Y., Jackson, R.A., and Thiery, J.P. (2016). EMT: 2016. *Cell* 166, 21–45.
- Nussbaum, E.S., Djallilian, H.R., Cho, K.H., and Hall, W.A. (1996). Brain metastases. Histology, multiplicity, surgery, and survival. *Cancer* 78, 1781–1788.
- Pan, C., Cai, R., Quacquarelli, F.P., Ghasemigharagoz, A., Loubopoulos, A., Matryba, P., Plesnila, N., Dichgans, M., Hellal, F., and Ertürk, A. (2016). Shrinkage-mediated imaging of entire organs and organisms using uDISCO. *Nat. Methods* 13, 859–867.
- Polyak, K., and Weinberg, R.A. (2009). Transitions between epithelial and mesenchymal states: acquisition of malignant and stem cell traits. *Nat. Rev. Cancer* 9, 265–273.
- Renier, N., Wu, Z., Simon, D.J., Yang, J., Ariel, P., and Tessier-Lavigne, M. (2014). iDISCO: a simple, rapid method to immunolabel large tissue samples for volume imaging. *Cell* 159, 896–910.
- Saadatpour, Z., Rezaei, A., Ebrahimnejad, H., Baghaei, B., Bjorklund, G., Chartrand, M., Sahebkar, A., Morovati, H., Mirzaei, H.R., and Mirzaei, H. (2017). Imaging techniques: new avenues in cancer gene and cell therapy. *Cancer Gene Ther.* 24, 1–5.
- Saito, R.A., Watabe, T., Horiguchi, K., Kohyama, T., Saitoh, M., Nagase, T., and Miyazono, K. (2009). Thyroid transcription factor-1 inhibits transforming growth factor-beta-mediated epithelial-to-mesenchymal transition in lung adenocarcinoma cells. *Cancer Res.* 69, 2783–2791.
- Shibue, T., Brooks, M.W., Inan, M.F., Reinhardt, F., and Weinberg, R.A. (2012). The outgrowth of micrometastases is enabled by the formation of filopodium-like protrusions. *Cancer Discov.* 2, 706–721.
- Spalteholz, W. (1914). Über das Durchsichtigmachen von menschlichen und tierischen Präparaten und seine theoretischen bedingungen, nebst Anhang (Leipzig: S Hierzel), pp. 1–93.
- Spiegel, A., Brooks, M.W., Houshyar, S., Reinhardt, F., Ardolino, M., Fessler, E., Chen, M.B., Krall, J.A., DeCock, J., Zervantonakis, I.K., et al. (2016). Neutrophils suppress intraluminal NK cell-mediated tumor cell clearance and enhance extravasation of disseminated carcinoma cells. *Cancer Discov.* 6, 630–649.
- Susaki, E.A., and Ueda, H.R. (2016). Whole-body and whole-organ clearing and imaging techniques with single-cell resolution: Toward organism-level systems biology in mammals. *Cell Chem. Biol.* 23, 137–157.
- Susaki, E.A., Tainaka, K., Perrin, D., Kishino, F., Tawara, T., Watanabe, T.M., Yokoyama, C., Onoe, H., Eguchi, M., Yamaguchi, S., et al. (2014). Whole-brain imaging with single-cell resolution using chemical cocktails and computational analysis. *Cell* 157, 726–739.
- Susaki, E.A., Tainaka, K., Perrin, D., Yukinaga, H., Kuno, A., and Ueda, H.R. (2015). Advanced CUBIC protocols for whole-brain and whole-body clearing and imaging. *Nat. Protoc.* 10, 1709–1727.
- Tainaka, K., Kubota, S.I., Suyama, T.Q., Susaki, E.A., Perrin, D., Ukai-Tadenuma, M., Ukai, H., and Ueda, H.R. (2014). Whole-body imaging with single-cell resolution by tissue decolorization. *Cell* 159, 911–924.
- Tainaka, K., Kuno, A., Kubota, S.I., Murakami, T., and Ueda, H.R. (2016). Chemical principles in tissue clearing and staining protocols for whole-body cell profiling. *Annu. Rev. Cell Dev. Biol.* 32, 713–741.
- Takahashi, K., Nagai, N., Ogura, K., Tsuneyama, K., Saiki, I., Irimura, T., and Hayakawa, Y. (2015). Mammary tissue microenvironment determines T cell-dependent breast cancer-associated inflammation. *Cancer Sci.* 106, 867–874.
- Tatsuki, F., Sunagawa, G.A., Shi, S., Susaki, E.A., Yukinaga, H., Perrin, D., Sumiyama, K., Ukai-Tadenuma, M., Fujishima, H., Ohno, R., et al. (2016). Involvement of Ca(2+)-dependent hyperpolarization in sleep duration in mammals. *Neuron* 90, 70–85.
- Tsai, J.H., and Yang, J. (2013). Epithelial-mesenchymal plasticity in carcinoma metastasis. *Genes Dev.* 27, 2192–2206.
- Tuchin, V.V. (2015). Tissue optics and photonics: Light-tissue interaction. *J. Biomed. Photonics Eng.* 1, 98–135.
- Yang, B., Treweek, J.B., Kulkarni, R.P., Deverman, B.E., Chen, C.K., Lubeck, E., Shah, S., Cai, L., and Gradinaru, V. (2014). Single-cell phenotyping within transparent intact tissue through whole-body clearing. *Cell* 158, 945–958.
- Ye, X., and Weinberg, R.A. (2015). Epithelial-mesenchymal plasticity: A central regulator of cancer progression. *Trends Cell Biol.* 25, 675–686.

Cell Reports, Volume 20

Supplemental Information

**Whole-Body Profiling of Cancer Metastasis
with Single-Cell Resolution**

**Shimpei I. Kubota, Kei Takahashi, Jun Nishida, Yasuyuki Morishita, Shogo Ehata, Kazuki
Tainaka, Kohei Miyazono, and Hiroki R. Ueda**

1 **Figure S1. Whole-body and whole-organ clearing and imaging with optimized RI solutions, Related to**
2 **Figure 1**

3 (A) Bright-field images of whole organs (pancreas and spleen) from C57BL/6N mouse (13 weeks old, male)
4 after RI adjustment (RI=1.44, 1.45, 1.46, 1.47, 1.48, 1.49, 1.50, 1.51, and 1.52). Control organs were stocked in
5 PBS buffer (RI=1.33). (B) Averaged parallel transmittance of RI adjusted organs. Averaged parallel
6 transmittance around the visible region (450-750 nm) of organs (heart, liver, kidney, pancreas, and spleen) was
7 measured (n=2). Data represent mean \pm SD. (C) Transmission curves around the visible region (450-750 nm) of
8 fixed whole organs (brain, heart, lung, liver, kidney, pancreas, and spleen) treated with the new CUBIC protocol
9 (CUBIC-L for delipidation and decoloring, and CUBIC-R for RI adjustment). (D) 3D (upper) and XY images
10 (lower) of the brain, heart, liver, and kidney from RedDot2-stained adult C57BL/6N mouse (15 week old, male).
11 (E) Magnified images in **Figure 1F**. 3D (middle) and XY images (left and right) of chest, abdomen, pancreas,
12 and intestine are shown. (F) The 3D-immunostained organ images with anti- α -SMA antibody and anti-VEGFR3
13 antibody. The lung from C57BL/6N mouse (13 week old, male) was co-immunostained with FITC-conjugated
14 anti- α -SMA antibody and anti-VEGFR3 antibody on the first staining step, and then with Alexa 647-conjugated
15 anti-mouse IgG antibody on the second staining step. 3D (upper) and XY images (lower) are shown. The white
16 inset was magnified next to the XY image.

17

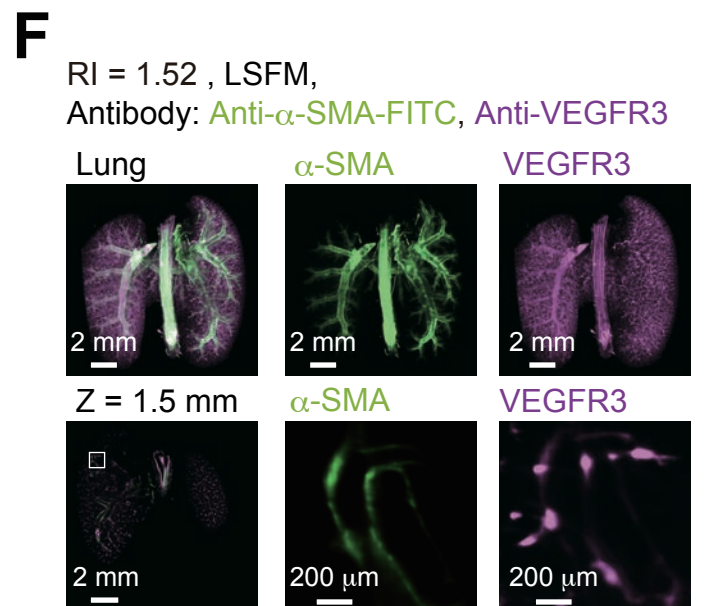
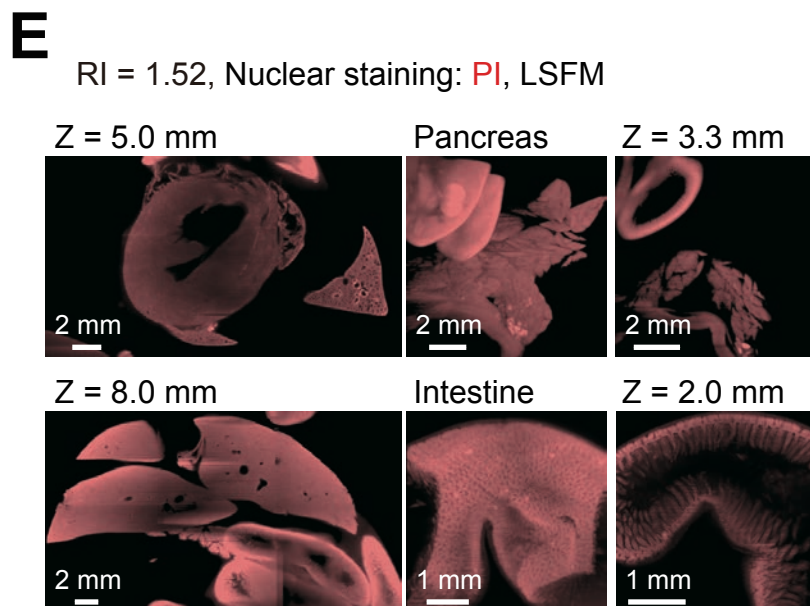
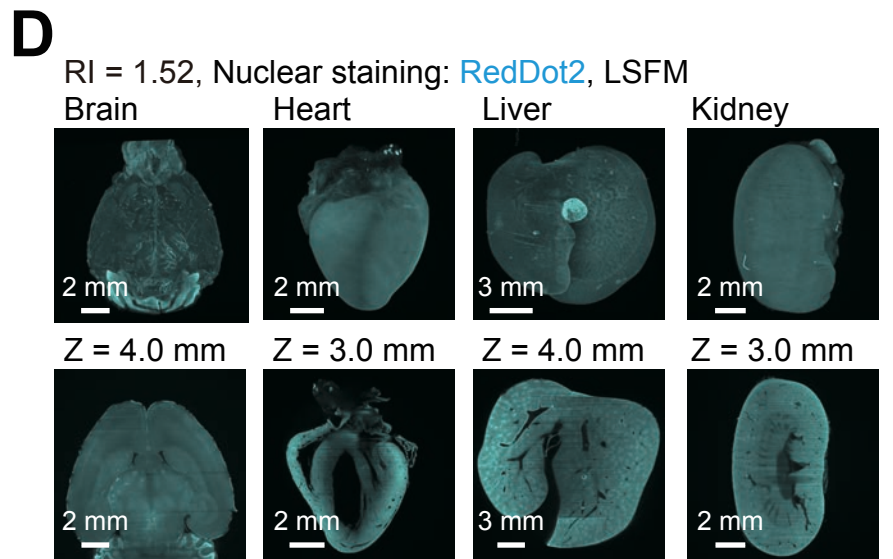
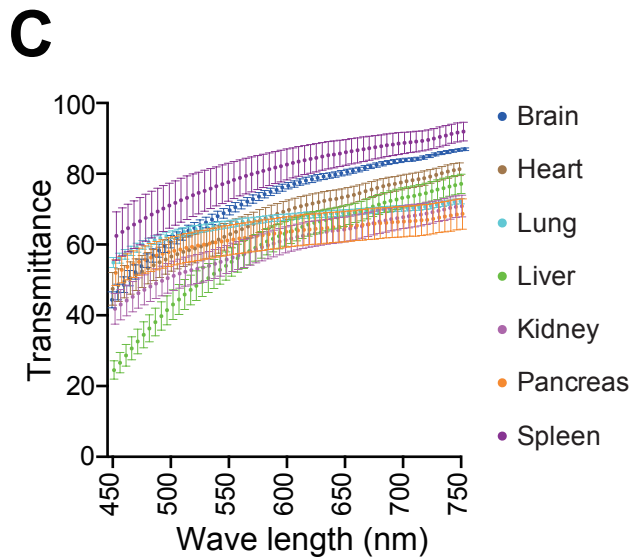
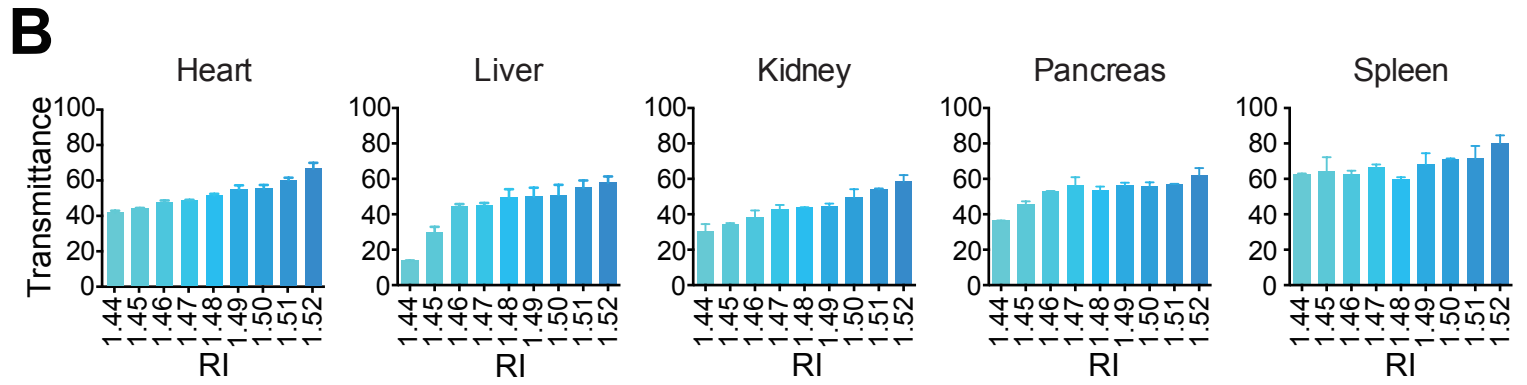
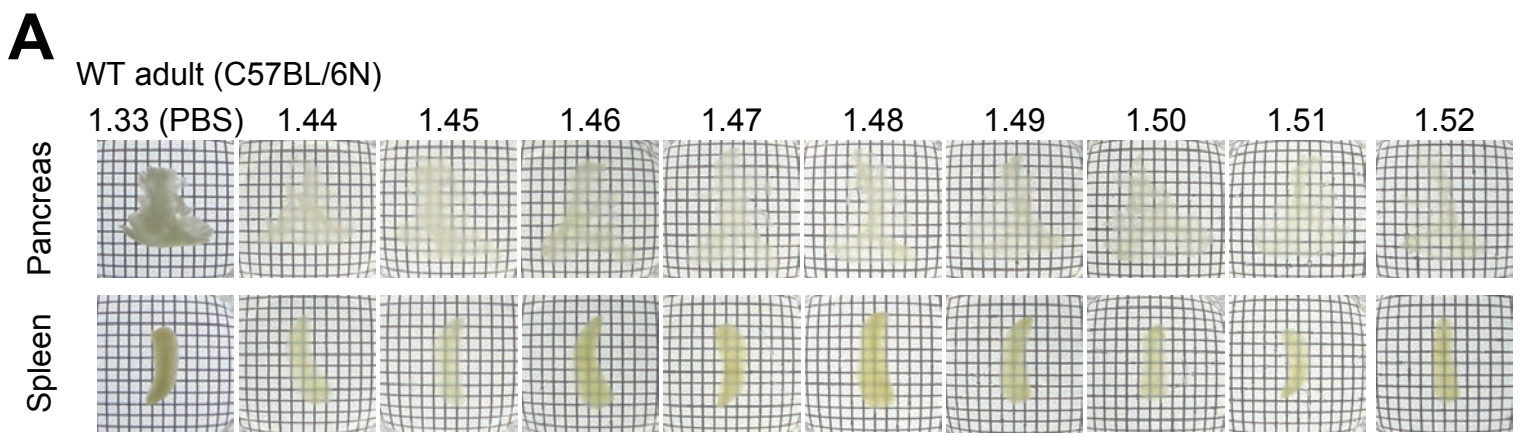


Figure S1

1 **Figure S2. Whole-body imaging of cancer metastasis, Related to Figure 2**

2 (A) *In vivo* bioluminescence imaging of **Figures 2C** and **2E**. (B) Whole-body imaging of the experimental
3 peritoneal dissemination model with SUIT-2 cells according to **Figure 2C**. WBI (left most), images of liver and
4 pancreas (LP), and intestine (I) (second left), and magnified images (right most) are shown (SUIT-2: GFP,
5 nuclei: PI). (C) Whole-body imaging of the experimental peritoneal dissemination model by intraperitoneal
6 injection with SUIT-2 cells in BALB/*c-nu/nu* mice. The bioluminescence image (left most), WBI (second left),
7 images of liver (L) and intestine (I) (third left) and magnified 3D and XY images (fourth left and right most) are
8 shown (SUIT-2: mCherry, nuclei: RedDot2). (D) Magnified images of pancreas and lymph nodes as shown in
9 **Figure 2E**. Images of pancreas (P) and lymph nodes (LN) (left most) and magnified 3D and XY images (second
10 left to right most) are shown (Renca: mCherry, nuclei: RedDot2). (E) Quantification of the cell number and the
11 volume of metastatic colonies. Spot analysis and surface analysis were applied to the magnified images in
12 **Figure S2D**.

13

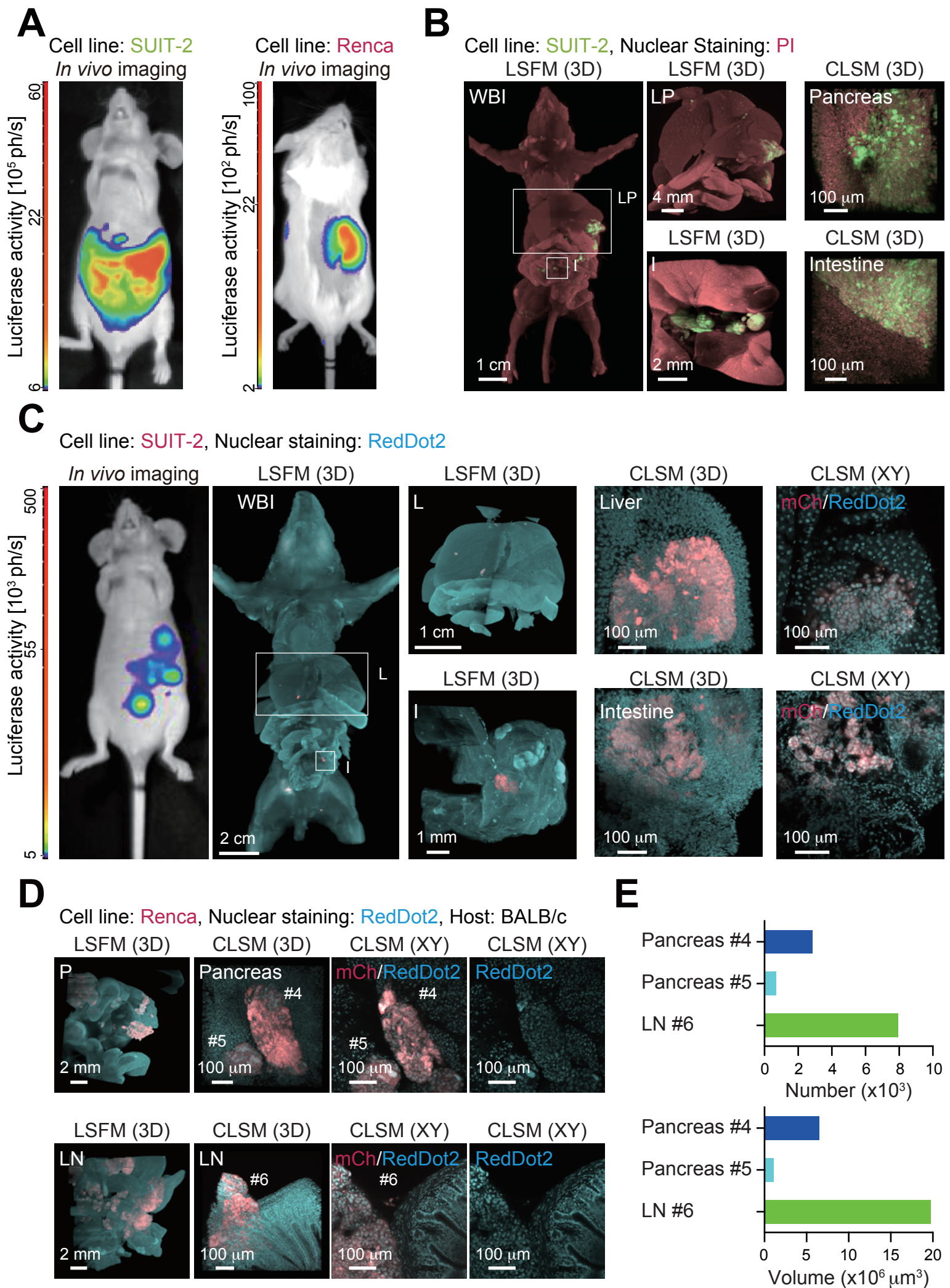
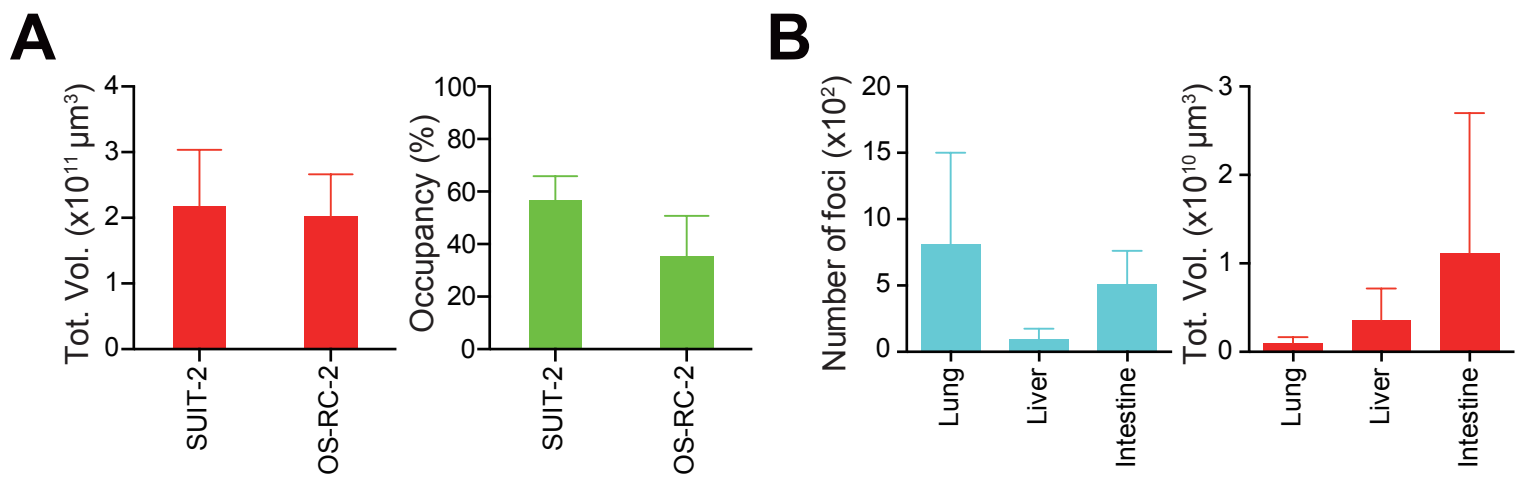


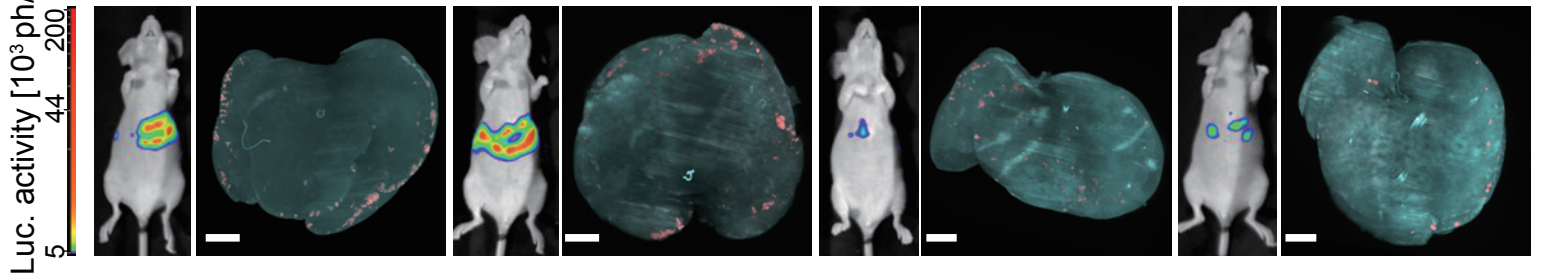
Figure S2

1 **Figure S3. Whole-organ imaging of various cancer metastasis models, Related to Figure 3**

2 (A) Quantification of the occupancy of the primary tumor in the primary organ in orthotopic models with
3 SUIT-2 cells and OS-RC-2 cells. Four to five weeks after injection, the volumes of primary tumors and organs
4 (SUIT-2: pancreas, OS-RC-2: kidney) were measured. The occupancies of the primary tumors are shown
5 (SUIT-2 cells: n=3, OS-RC-2: n=4). Data represent mean \pm SD. (B) Quantification of the number and the total
6 volume of metastatic foci in the experimental metastasis model with SUIT-2 cells as shown in **Figure 3B**.
7 Surface analysis was applied to the whole-organ images. The number and total volume of metastatic foci in the
8 organs are shown (SUIT-2 cells: n=3). Data represent mean \pm SD. (C) Whole-liver imaging of the experimental
9 liver metastasis model with Panc-1 cells. Images of *in vivo* bioluminescence and whole liver images by CUBIC
10 are shown (Panc-1: mCherry, nuclei: RedDot2) (n=4). (D) Confirmation of the specific detection of cancer cells
11 in the CUBIC-Cancer analysis by merged images of a red channel from mCherry-expressing cancer cells and
12 far-red channel from Alexa Fluor 647-conjugated anti-mCherry antibody staining. The 3D images of lung, brain,
13 and pancreas from the 4T1 metastasis model mouse immunostained with Alexa Fluor 647-conjugated
14 anti-mCherry antibody are shown (4T1: mCherry, anti-mCherry: Alexa Fluor 647).
15



C Cell line: **Panc-1**, Nuclear staining: **RedDot2**, Scale bar: 2 mm, LSMF



D Cell line: **4T1**, Antibody: **Anti-mCherry-Alexa Fluor 647 antibody**, Scale bar: 2 mm, LSMF

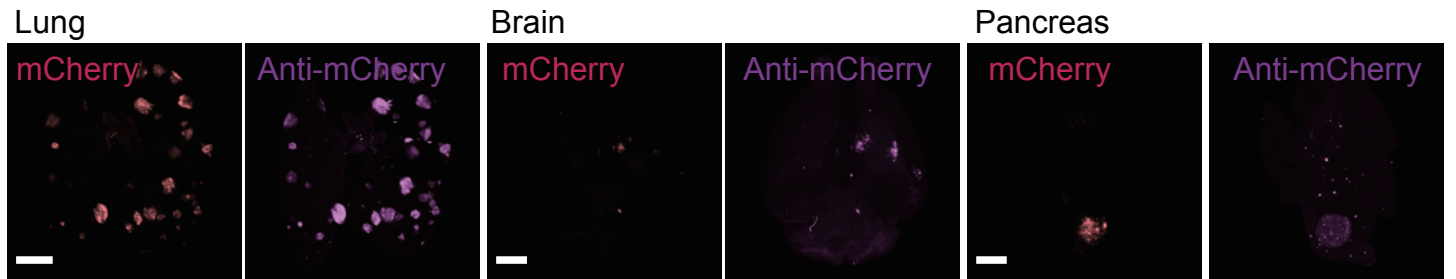


Figure S3

1 **Figure S4. 3D analysis of the metastatic patterns in experimental brain metastasis models, Related to**

2 **Figure 4**

3 (A) *In vivo* bioluminescence imaging of brain metastasis. Representative images of the brain metastasis are
4 shown (left: MDA-231-D, right: OS-RC-2). (B) HE staining of the samples after CUBIC-Cancer analysis or
5 normal samples. Representative images of the brain metastasis are shown (MDA-231-D: left, OS-RC-2: right,
6 normal sample: upper, sample after CUBIC-Cancer analysis: lower). (C) Whole-brain analysis of the distribution
7 of metastatic volume and distance from blood vessel. Surface analysis and spot analysis were applied to the 3D
8 images in **Figure 4B**. Data represent mean \pm SD.

9

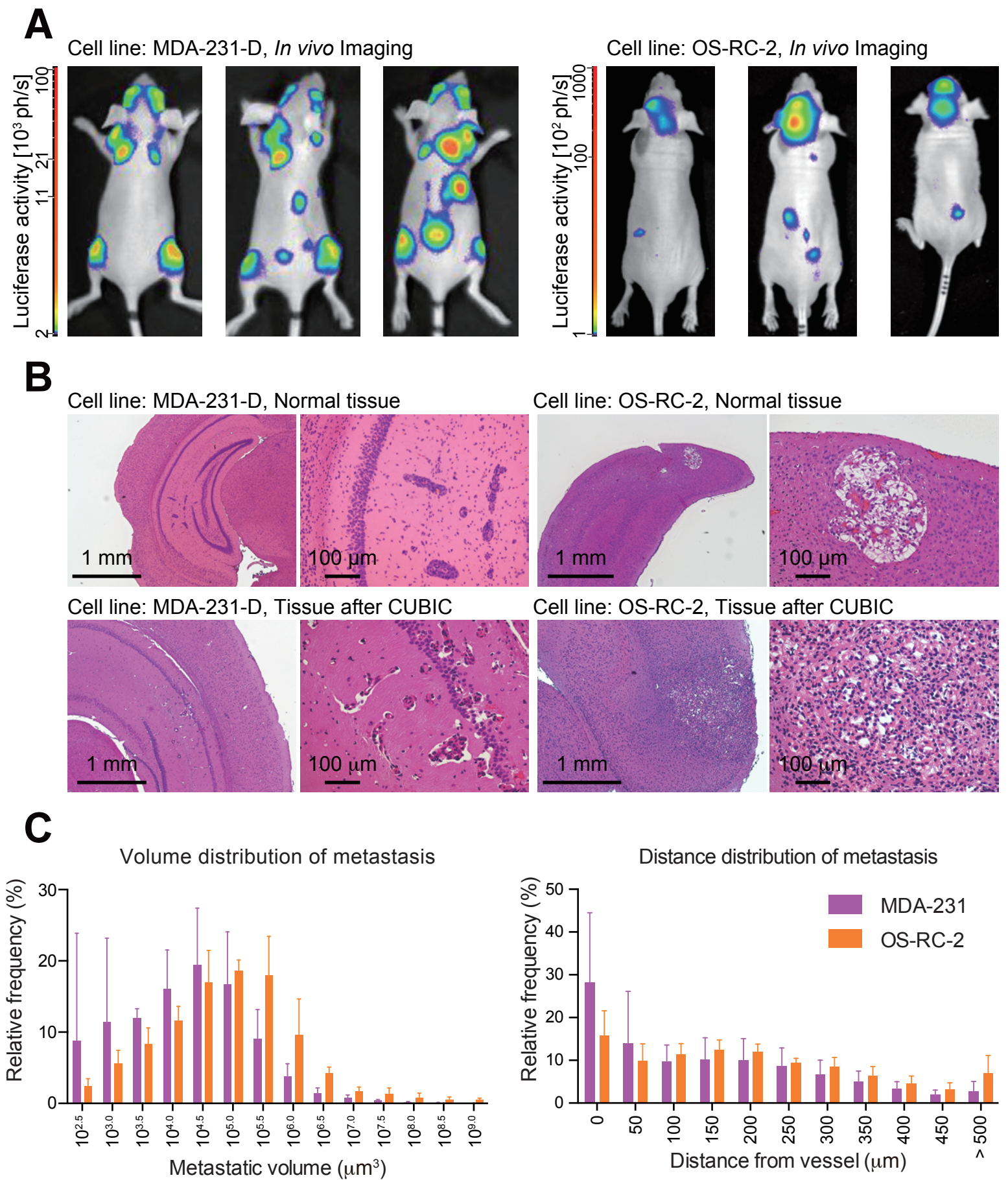
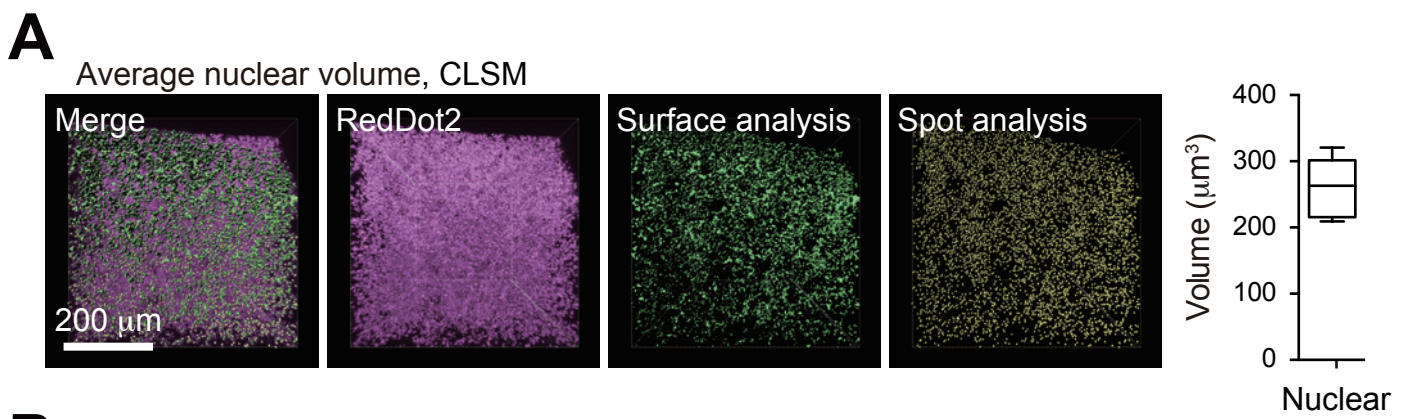


Figure S4

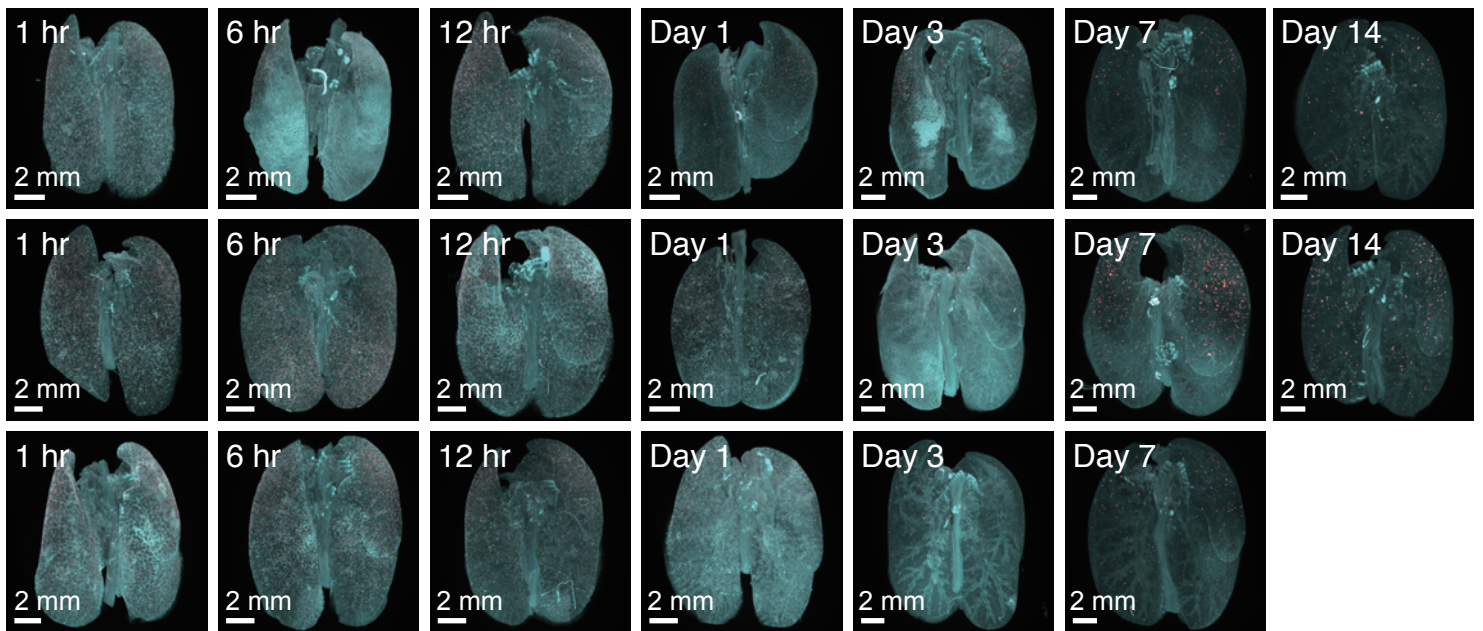
1 **Figure S5. Spatio-temporal dynamics of experimental lung metastasis, Related to Figure 5**

2 (A) Determination of the minimum threshold for the metastatic focus count. The volume of individual metastatic
3 foci is postulated to be larger than the nuclear volume. To quantify the pulmonary nuclear volume in the
4 RedDot2-stained lung, surface analysis and spot analysis were applied to the 3D lung images acquired with
5 CLSM. The averaged nuclear volume of six fields (right most) is shown. (B, C) Time course images of the
6 experimental lung metastasis model with MDA-231-D cells in BALB/*c-nu/nu* mice (B) and BALB/*c* mice (C).
7 The three or two additional individual mice were analyzed by CUBIC-Cancer analysis according to **Figures 5B**
8 and **5C**. (MDA-231-D: mCherry, nuclei: RedDot2). These images were further analyzed with Imaris software in
9 **Figures 5D, 5E, 5F, and 5G**.

10



B Cell line: MDA-231-D, Nuclear staining: RedDot2, Host mouse: BALB/c-*nu/nu* mouse, LSFM



C Cell line: MDA-231-D, Nuclear staining: RedDot2, Host mouse: BALB/c mouse, LSFM

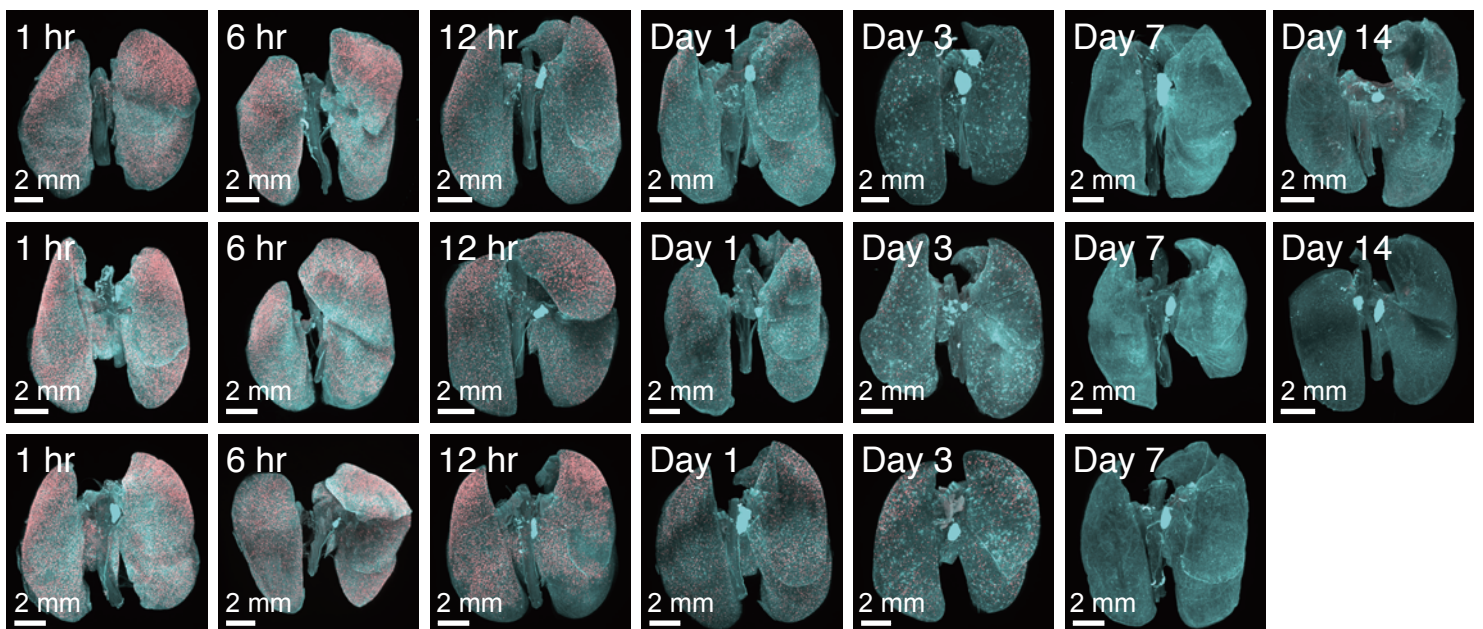
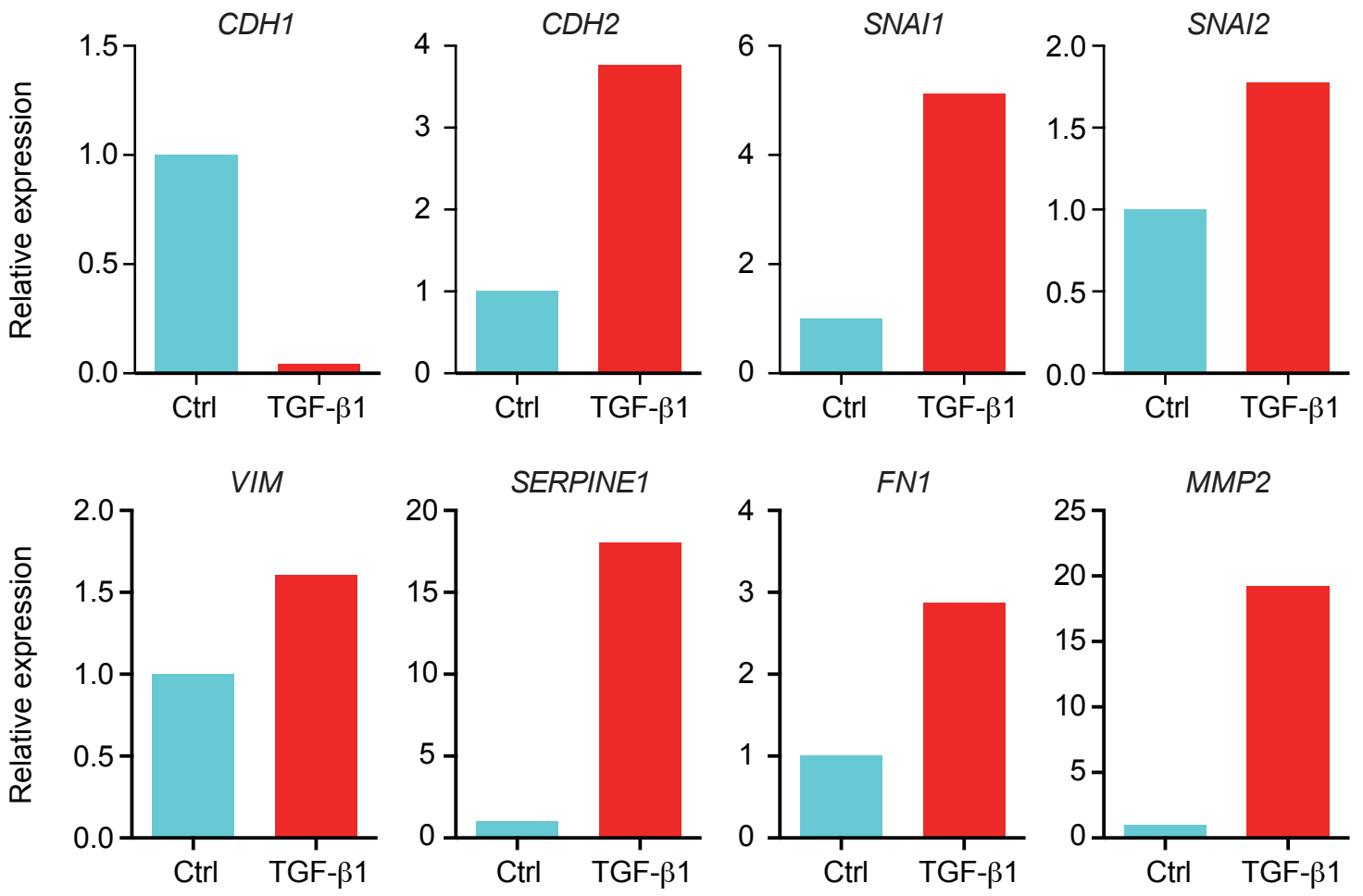
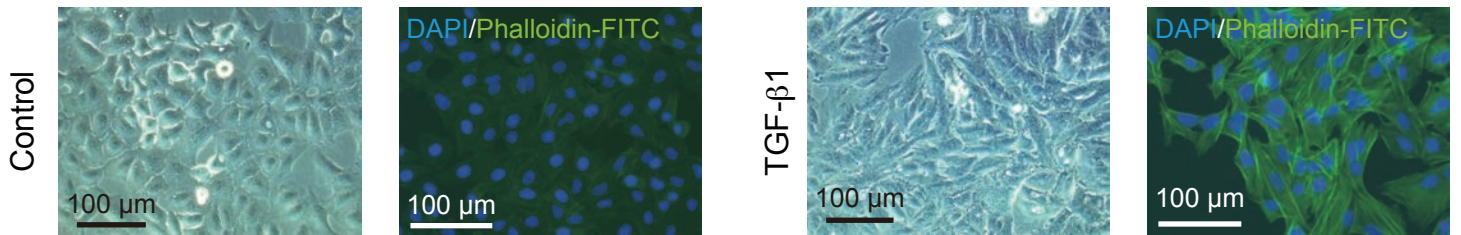


Figure S5

1 **Figure S6. Role of EMT induced by TGF- β during lung metastasis, Related to Figure 6**

2 (A) Expression of EMT markers in A549 cells. A549 cells were stimulated with or without TGF- β 1 (5 ng/ml) for
3 3 days. Relative expression levels of each gene are shown. All data are presented as mean (duplicate). (B)
4 FITC-conjugated phalloidin staining of A549 cells. A549 cells were stimulated with or without TGF- β 1 (5
5 ng/ml) for 3 days. Formation of the F-actin was evaluated by phalloidin staining.

6

A**B****Figure S6**

1 **Table S1. List of mouse tumor models in the present study, Related to Figure 2**

2 9 cancer cell lines and 13 mouse tumor models were used in this study. Source of cancer cells, type of cancer,
 3 injection protocol, and organs for metastasis are described.

Cell	Source	type	injection	host mouse	metastasis	Figure
MDA-MB-231-Luc2- 2-mCherry/ MDA-231-D-Luc2- mCherry	human	breast cancer	intravenous (i.v.) (1 hr-6 w)	BALB/c- <i>nu/nu</i> , BALB/c	lung	3C, 5, S5
MDA-231-D-Luc2- mCherry	human	breast cancer	intracardiac (i.c.) (4 w)	BALB/c- <i>nu/nu</i>	bone, brain	4, S4
A549-Luc2- mCherry	human	lung cancer	i.v. (1 hr-4 w)	BALB/c- <i>nu/nu</i>	lung	3C, 6
OS-RC-2-Luc2- GFP/ OS-RC-2-Luc2- mCherry	human	renal carcinoma	i.c. (5-7 w)	BALB/c- <i>nu/nu</i>	brain, bone	4, S4
OS-RC-2-Luc2-GF P	human	renal carcinoma	orthotopic (4 w)	BALB/c- <i>nu/nu</i>	lung	S3A
Caki-1-Luc2- mCherry	human	renal carcinoma	orthotopic (14 w)	BALB/c- <i>nu/nu</i>	lung	3C, 3D
SUIT-2-Luc2-GFP/ SUIT-2-Luc2- mCherry	human	pancreatic cancer	intra- peritoneal (i.p.) (1-3 w)	BALB/c- <i>nu/nu</i>	peritoneum	2C, 2D, S2A, S2B, S2C
SUIT-2-Luc2- mCherry	human	pancreatic cancer	orthotopic (5 w)	BALB/c- <i>nu/nu</i>	lung, liver, peritoneum	3B, S3A, S3B
Panc-1-Luc2-GFP/ Panc-1-Luc2-	human	pancreatic cancer	splenic (4-9 w)	BALB/c- <i>nu/nu</i>	liver	2B, S3C

mCherry						
4T1-mCherry	mouse	breast cancer	i.v. (2 w)	BALB/c- <i>nu/nu</i>	lung	3C, S3D, 7
B16F10-mCherry	mouse	melanoma	i.v. (2 w)	C57/B6	lung	3C, 3D
Renca-Luc2- mCherry	mouse	renal carcinoma	i.v. (3 w)	BALB/c	lung	3C
Renca-Luc2- mCherry	mouse	renal carcinoma	orthotopic (2 w)	BALB/c	lung, peritoneum	2E, 2F, S2A, S2D, S2E

1

2

1 **Table S2. List of the name of CUBIC solutions**

2 We developed four clearing solutions as below.

Name	Key ingredients	References
Sca/eCUBIC-1	Urea, Quadrol, Triton X-100	Susaki et al., 2014, Tainaka et al., 2014, Susaki et al., 2015
Sca/eCUBIC-2	Urea, Sucrose, Triethanolamine	Susaki et al., 2014, Tainaka et al., 2014, Susaki et al., 2015
CUBIC-L	N-buthyldiethanolamine, Triton X-100	Present study
CUBIC-R	Nicotinamide, Antipyrine	Present study

3

1 **Table S3. Antibodies used in the present study**

2 Indicated antibodies were used for immunostaining in the present study.

Antibody	Catalog number	Company
FITC-conjugated anti- α -smooth muscle actin (α -SMA) antibody	F3777	Sigma-Aldrich
Anti-VEGFR3/Flt-4 antibody	AF743	R&D Systems
Alexa Fluor 647 AfiiniPure Fab Fragment Bovine Anti-Goat IgG, Fc fragment specific	805-607-008	Jackson ImmunoResearch Laboratories
Alexa Fluor 647 conjugated anti-mCherry antibody (16D7)	M11241	Thermo Fischer Scientific
Anti-E-cadherin (24E10) antibody	#3195	Cell Signaling Technology

3

4

1 **Table S4. Primer sequences used in the present study**

2 Indicated primers were used for qRT-PCR analysis in the present study.

Gene	Orientation	Sequence (5' to 3')
<i>HPRT1</i>	Forward	TTTGCTTTCCTTGGTCAGGC
	Reverse	GCTTGCGACCTTGACCATCT
<i>CDH1</i>	Forward	ATTTTTCCTCGACACCCGAT
	Reverse	TCCCAGGCGTAGACCAAGA
<i>CDH2</i>	Forward	TTCCTTGCTTCTGACAATGG
	Reverse	ATGTCATAATCAAGTGCTG
<i>SNAI1</i>	Forward	ACTGCAGCCGTGCCTTCG
	Reverse	GTGCTTGTGGAGCAGGGACAT
<i>SNAI2</i>	Forward	GCCTCCAAAAAGCCAAACTACA
	Reverse	GAGGATCTCTGGTTGTGGTATGACA
<i>VIM</i>	Forward	GAGAACTTTGCCGTTGAAGC
	Reverse	TGGTATTCACGAAGGTGACG
<i>SERPINE1</i>	Forward	GGCTGACTTCACGAGTCTTCA
	Reverse	ATGCGGGCTGAGACTATGACA
<i>FNI</i>	Forward	CTGGCCGAAAATACATTGTAAA
	Reverse	CCACAGTCGGGTCAGGAG
<i>MMP2</i>	Forward	TGGCGATGGATACCCCTTT
	Reverse	TTCTCCCAAGGTCCATAGCTCAT

3

4

EXTENDED EXPERIMENTAL PROCEDURES

Preparation of Clearing Solutions

Compared with previous CUBIC solutions, the viscosity of CUBIC-L and CUBIC-R is relatively low. Although the water content of CUBIC-R is low to achieve high RI, CUBIC-R is unlikely to precipitate and easy to handle. N-methylnicotinamide (M0374, Tokyo Chemical Industry Co., Ltd.) is an alternative chemical for nicotinamide, and used in Figure 1G, S1D, S1F, 3C (MDA-MB-231), 4 (MDA-231-D).

The CUBIC Protocol for Whole-body and Whole-organ Clearing

For the preparation of whole-organ clearing samples, adult mice (C57BL/6N) were sacrificed by an overdose of pentobarbital (> 100 mg/kg, Kyoritsu Seiyaku, Tokyo, Japan) and then perfused with 20 ml of PBS (pH 7.4) and 30 ml of 4% (w/v) PFA (02890-45, Nacalai Tesque) in PBS via left ventricle of the heart. The excised organs were post-fixed in 4% (w/v) PFA at 4°C for 24 hours. The specimens were washed with PBS for more than 2 hours three times to remove PFA just before clearing. The fixed organs were immersed in 50% (v/v) CUBIC-L (1:1 mixture of water and CUBIC-L) for more than 6 hours and further immersed in CUBIC-L with gentle shaking at 37°C for 2-5 days, depending on the organs (typically 3 days for the heart, lung, intestine, pancreas, and spleen, and 5 days for the brain, liver, and kidney). CUBIC-L should be daily refreshed during the procedure. After decolorization and delipidation, the organs were washed with PBS at room temperature for more than 2 hours three times. The organs were further immersed in 50% (v/v) CUBIC-R (1:1 mixture of water and CUBIC-R) for more than 6 hours, and then in CUBIC-R at room temperature with gentle shaking for at least 1 day.

For the preparation of whole-body clearing samples, anesthetized mice were perfused with 30 ml of PBS, 150 ml of 4% (w/v) PFA in PBS, 20 ml of PBS, and 100 ml of 50% (v/v) CUBIC-L in this order via left ventricle of the heart. The mice were immersed in 200 ml of 50% (v/v) CUBIC-L at 37°C for more than 6 hours, and further immersed in CUBIC-L at 37°C with gentle shaking for at least 5 days. After decolorization and delipidation, mice were washed with PBS at room temperature for 1 day. Mice were further immersed in 50% CUBIC-R for 1 day, and then in CUBIC-R at room temperature with gentle shaking for at least 1 day. Although bone tissues, gastrointestinal tissues, brown adipose tissues, and eyeball were still difficult to be transparentized

1 in this protocol, it was sufficiently clear enough to execute whole-body and whole-organ scanning of cancer
2 metastasis. Expressed proteins are expected to be stably conserved even after clearing procedure, while RNA
3 may be fully degraded in alkaline CUBIC-L treatment.

4 5 **3D Nuclear Staining of CUBIC Samples**

6 For nuclear staining with propidium iodide (PI), whole-body samples were subjected to nuclear staining with 5
7 $\mu\text{g/ml}$ PI during decolorization and delipidation at 37°C with shaking for 7 days. For nuclear staining with
8 RedDot2, whole-body/organ samples were subjected to nuclear staining with 1:100 diluted RedDot2 after
9 decolorization and delipidation at room temperature with shaking for 3 to 7 days.

10 11 **3D Immunostaining of CUBIC Samples**

12 Organ samples after decolorization and delipidation were subjected to immunostaining with the 1:100 diluted
13 antibodies in the staining buffer composed of 0.5% (v/v) Triton X-100, 0.25% casein (37528, Thermo Fisher
14 Scientific, Waltham, MA), and 0.01% sodium azide (31208-82, Nacalai Tesque) for 3 to 5 days at room
15 temperature with shaking. The stained samples were washed with PBS three times at room temperature with
16 rotation, and then immersed in CUBIC-R. The following antibodies were used for the staining (**Table S3**):
17 FITC-conjugated anti- α -smooth muscle actin (α -SMA) antibody produced in mouse (F3777, Sigma-Aldrich) for
18 the brain, heart, lung, liver, kidney, pancreas, and spleen, mCherry antibody (16D7) Alexa Fluor 647 conjugate
19 (M11241, Thermo Fisher Scientific) for the brain, lung, pancreas, Mouse VEGFR3/Flt-4 antibody (AF743, R&D
20 Systems, Minneapolis, MN), and Alexa Fluor 647 AffiniPure Fab Fragment Bovine Anti-Goat IgG, Fc fragment
21 specific (805-607-008, Jackson ImmunoResearch Laboratories, West Grove, PA).

22 The magnified images in Figure 1G and S1F clearly showed the separated punctate signals and luminal
23 signals. Regarding the detected red-color signals in cancer cells, we confirmed their signals by immunostaining
24 with anti-mCherry antibody. In Figure 3D and S3D, the red-colored signals totally matched with the
25 immunostaining signals from anti-mCherry antibody.

26

1 **Microscopy**

2 Whole-body and whole-organ images were acquired with a custom-build LSM (developed by Olympus, Tokyo,
3 Japan). Images were captured at 0.63 × objective lens (numerical aperture = 0.15, working distance = 87 mm) with
4 digital zoom from 1 × to 6.3 × zoom. Lasers of 488 nm, 532 nm, 590 nm, and 639 nm were used for image
5 acquisition. To cover whole-body or whole-organs, the stage was moved both in the lateral direction and axial
6 direction. When the stage was moved to the axial direction, the detection objective lens was synchronically moved
7 to the axial direction to avoid defocusing. High resolution images for cell profiling were acquired with CLSM
8 (FLUOVIEW FV1200, Olympus). Images were captured at 25 × objective lens (numerical aperture = 1.0,
9 working distance = 8.0 mm) with digital zoom from 1 × to 2 × zoom. Lasers of 473 nm, 559 nm, and 635 nm were
10 used for image acquisition. RI matched sample was immersed in a mixture of silicon oil HIVAC-F4 (RI = 1.555,
11 Shin-Etsu Chemical Co., Ltd., Tokyo, Japan) and mineral oil (RI = 1.467, M8410, Sigma-Aldrich) during image
12 acquisition. 3D-rendered images were visualized, captured and analyzed with Imaris software (version 7.7.1 and
13 8.1.2, Bitplane AG, Zurich, Switzerland).

14

15 **RI Matching Cocktails Composed of Antipyrine and Nicotinamide for RI Optimization of Each Organ**

16 We prepared RI matching cocktails composed of antipyrine and nicotinamide for the purpose of discovering the
17 optimized RI value for each organ. Cocktails with the RI ranging from 1.44 to 1.47 were adjusted only by
18 antipyrine concentration. Cocktails with the RI ranging from 1.48 to 1.49 were adjusted by antipyrine
19 concentration under the 10 wt% concentration of nicotinamide. Cocktails with the RI ranging from 1.50 to 1.51
20 were adjusted by antipyrine concentration under the 20 wt% concentration of nicotinamide. The cocktail with the
21 RI of 1.52 was composed of 45 wt%/30 wt% antipyrine/nicotinamide. PFA-fixed organs were decolorized and
22 delipidated by CUBIC-L for 5 days. After decolorization and delipidation, the organs were washed with PBS at
23 room temperature overnight. Then, the organs were further immersed in 50% CUBIC-R for 6 hours, and in the
24 prepared RI matching cocktails or PBS at room temperature with gentle shaking for 2 days.

25

26 **Measurement of Light Transmittance**

27 We measured light transmittance of the brain, heart, lung, liver, kidney, pancreas and spleen samples from 450 to
28 750 nm (in **Figures 1C, S1B, and S1C**) at 5 nm intervals with an integrating sphere (Spectral Haze Meter SH

1 7000, Nippon Denshoku Industries Co., Ltd., Tokyo, Japan). Every sample was embedded in the gel matrix
2 composed of CUBIC-R containing 2% agarose (318-001195, Wako Pure Chemical Industries, Ltd., Osaka,
3 Japan) inside the optical cell. The averaged parallel transmittance was measured. Trends in the increase of
4 transmittance against RI were different among organs. Lung and liver displayed a sharp increase of transmittance
5 below RI of 1.46, whereas transmittance of the brain, heart, and kidney were gradually increased over the
6 experimental RI range, suggesting that transparency of the former organs was a major determinant of the RI
7 matching step.

8

9 **Image Data Processing and Analysis**

10 All raw image data were collected in a lossless 16-bit TIFF format. 3D-rendered images were visualized and
11 captured with Imaris software (version 7.6.4, 7.7.1 and 8.1.2, Bitplane). Brightness, contrast, and gamma of the
12 3D-rendered images were manually adjusted with the software at minimum when visualized. The 3D images
13 were then used for image analysis with Imaris software. For the quantification of cancer metastasis, appropriate
14 threshold of signals from reporter proteins was selected in each experiment and surface analysis was performed
15 with Imaris software. To count cell number, appropriate threshold of signals from nuclear counterstaining was
16 selected in each experiment and spot analysis was performed with Imaris software. To quantify the
17 morphological features, we introduced the index of “volume per surface area” (the volume of the colony divided
18 by the surface area of the colony), which was positively correlated with the roundness of the colony in Figure 4C.
19 Noise signals such as hair of mouse were manually excluded with the software at minimum when visualized.

20

21 **Cancer Cells**

22 Human breast cancer cells, MDA-MB-231-5a-D (MDA-231-D), are a highly metastatic clone from
23 MDA-MB-231 (Ehata et al., 2007). Human renal cancer cells, OS-RC-2 and Caki-1, were kindly provided by
24 Prof. Tatsuhiro Irimura (Juntendo University, Tokyo, Japan) and Dr. Isaiah J Fidler (MD Anderson Cancer Center,
25 TX), respectively. SUIT-2 (Japanese Cancer Research Resource Bank, Osaka, Japan), Panc-1 (American Type
26 Culture Collection (ATCC), Manassas, VA), A549, MDA-MB-231, MDA-231-D, and B16F10 (ATCC) cells
27 were cultured in Dulbecco’s modified Eagle’s medium (DMEM) supplemented with 10% fetal bovine serum
28 (FBS), 50 U/ml penicillin and 50 µg/ml streptomycin as previously described (Hoshino et al., 2015). Renca
29 (ATCC), 4T1 (ATCC), and OS-RC-2 cells were maintained in RPMI1640 containing 10% FBS and

1 penicillin/streptomycin (Hoshino et al., 2011). Caki-1 cells were maintained in minimum essential medium
2 (MEM) containing 10% FBS and penicillin/streptomycin.

3

4 **Establishment of Cancer Cells Stably Expressing Luciferase and mCherry/GFP**

5 To establish cancer cells stably expressing firefly luciferase and mCherry/GFP under CMV or EF-1 promoter,
6 we used a lentiviral expression system (kindly provided by Dr Hiroyuki Miyoshi, RIKEN, Saitama, Japan). To
7 prepare the expression vectors, firefly luciferase gene (originated from pGL4.10, Promega, Madison, WI), GFP
8 gene and mCherry gene (originated from pmCherry, Clontech Laboratories, Inc., Mountain View, CA) were
9 inserted into the entry vector (pENTR201). Recombination between pENTR201 and destination vector
10 (CSII-CMV-RfA, CSII-EF-RfA) was performed with Gateway LR Clonase II enzyme (Thermo Fischer
11 Scientific). As a GFP expression vector, CS-CDF-CG-PRE was also used. 293FT cells were transfected with
12 vector constructs encoding each protein, the VSV-G and Rev expressing construct (pCMV-VSV-G-RSV-Rev),
13 and the packaging construct (pCAG-HIVgp). The culture supernatants containing viral particles were collected
14 and used as lentivirus vectors.

15

16 **Experimental and Spontaneous Mouse Metastatic Tumor Models**

17 Each metastasis model is described briefly as follows. For experimental liver metastasis, BALB/*c-nu/nu* mice (5
18 weeks old, female) were injected with Panc-1 cells ($0.5-1 \times 10^6$ cells/mouse) by open injection in the spleen.
19 Five minutes after injection, the spleen was surgically resected. For peritoneal dissemination, SUIT-2 cells were
20 injected into pancreas orthotopically (5×10^5 cells/mouse) or intraperitoneally (i.p.) (2×10^5 cells/mouse) in
21 BALB/*c-nu/nu* mice (5 weeks old, female). In the experimental liver metastasis model with Panc-1 cells and the
22 peritoneal dissemination model with SUIT-2 cells, mice were fed with OpenSource Diets (D10001, ESP
23 EKISHIN Co., Ltd., Tokyo, Japan) to reduce autofluorescence from intestine. For experimental lung metastasis
24 by intravenous (i.v.) injection, BALB/*c-nu/nu* (5 weeks old, female) or BALB/*c* mice (5 weeks old, female: 4T1,
25 male: Renca) or C57BL/6 mice (5 weeks old, female) were injected with each cell line (MDA-MB-231: 5×10^5
26 cells/mouse, MDA-231-D: 3×10^5 cells/mouse, A549: 1×10^6 cells/mouse, 4T1: $1.5-5 \times 10^5$ cells/mouse, Renca:
27 1×10^5 cells/mouse, B16F10: 2×10^5 cells/mouse). For spontaneous lung metastasis by renal subcapsule
28 injection, BALB/*c* (5 weeks old, male) or BALB/*c-nu/nu* mice (5 weeks old, male) were injected with Renca,
29 OS-RC-2 or Caki-1 cells orthotopically (Renca: 1×10^5 cells/mouse, OS-RC-2: 1×10^5 cells/mouse, Caki-1: $1 \times$

1 10^5 cells/mouse). For experimental brain metastasis by intracardiac (i.c.) injection, BALB/c-*nu/nu* mice (4 weeks
2 old, female: MDA-231-D, male: OS-RC-2) were injected with MDA-231-D or OS-RC-2 cells (MDA-231-D: $1-5$
3 $\times 10^5$ cells/mouse, OS-RC-2: 1×10^5 cells /mouse) by puncture into the left ventricle of heart. Mice were
4 sacrificed at 5 or 6 weeks after injection. For the stimulation with TGF- β , A549 cells were pre-treated with or
5 without TGF- β 1 (5 ng/ml) for 72 hours in culture. After the stimulation with TGF- β *in vitro*, cells were
6 harvested and inoculated intravenously (1×10^6 cells /mouse) in BALB/c-*nu/nu* mice (5 weeks old, female).

7

8 **Anti-tumor Drug Administration *In Vivo***

9 One day after 4T1 i.v. injection ($1.5-3 \times 10^5$ cells/mouse), mice were administered with an anti-tumor drug in a
10 protocol as described previously (Bao et al., 2011). Briefly, mice were injected with doxorubicin (Dox, 5 mg/kg
11 body weight, Toronto Research Chemicals, Toronto, Canada), 5-FU (35 mg/kg body weight, Nacalai Tesque) or
12 cyclophosphamide (CPA, 40 mg/kg body weight, Nacalai Tesque) intraperitoneally every other day (Day 1, 3, 5,
13 and 7). On Day 8, mice were sacrificed. In continuous administration, mice were injected with 5-FU (35 mg/kg
14 body weight) every day (Day 1-10). On Day 11, mice were sacrificed. Each drug was dissolved in saline (Otsuka
15 Pharmaceutical Factory, Inc., Tokushima, Japan). Mice in control groups were injected with saline.

16

17 ***In Vivo* Bioluminescence Imaging**

18 Mice were anesthetized with avertin and injected intraperitoneally with D-luciferin potassium salt (Promega).
19 Ten to fifteen minutes after injection, luciferase activity was measured using NightOWL II LB983 (Berthold
20 Technologies GmbH & Co. KG, Bad Wildbad, Germany).

21

22 **Histological Examination**

23 After CUBIC-Cancer analysis, whole liver, brain and lung were washed with PBS and resected. The samples
24 were embedded in paraffin and subjected to HE staining as previously described (Hoshino et al., 2015).

25

26 **Immunohistochemistry**

27 Immunohistochemistry was performed with VECTASTAIN Elite ABC Kit (Vector Laboratories Inc.,
28 Burlingame, CA). Samples after CUBIC-Cancer analysis in PBS were embedded in paraffin. Anti-E-cadherin
29 (24E10) antibody was purchased from Cell Signaling Technology (Danvers, MA).

1

2 **RNA Isolation and qRT-PCR Analysis**

3 Total RNA was extracted with Isogen reagent (Nippon Gene, Toyama, Japan). cDNA was synthesized using
4 PrimeScript II 1st strand cDNA Synthesis Kit (Takara, Otsu, Japan) according to the manufacturer's protocol.
5 Gene expression was analyzed with StepOne Plus Real time-PCR System (Life Technologies, Carlsbad, CA) and
6 Fast SYBR Green Master Mix with ROX (Roche Diagnostics, Tokyo, Japan). The expression level of each gene
7 was normalized to that of hypoxanthine-guanine phosphoribosyltransferase (*HPRT1*). Primer sequences are
8 shown in **Table S4**.

9

10 **Phalloidin Staining**

11 A549 cells were stimulated with or without TGF- β 1 (5 ng/ml) for 3 days. After the stimulation, cells were fixed
12 with 4% formaldehyde solution and permeabilized with 0.1% Triton-X. Cells were stained with
13 FITC-conjugated phalloidin (P5282, Sigma-Aldrich). Cell nuclei were stained with DAPI (Vector Laboratories
14 Inc.). Images were captured with All-in-One fluorescence microscope BZ-X710 (KEYENCE, Osaka, Japan).

15

1 SUPPLEMENTAL REFERENCES

2

3 Bao, L., Haque, A., Jackson, K., Hazari, S., Moroz, K., Jetly, R., and Dash, S. (2011). Increased expression of
4 P-glycoprotein is associated with doxorubicin chemoresistance in the metastatic 4T1 breast cancer model. *Am J*
5 *Pathol* 178, 838-852.

6 Ehata, S., Hanyu, A., Fujime, M., Katsuno, Y., Fukunaga, E., Goto, K., Ishikawa, Y., Nomura, K., Yokoo, H.,
7 Shimizu, T., *et al.* (2007). Ki26894, a novel transforming growth factor- β type I receptor kinase inhibitor,
8 inhibits in vitro invasion and in vivo bone metastasis of a human breast cancer cell line. *Cancer Sci* 98, 127-133.

9 Hoshino, Y., Katsuno, Y., Ehata, S., and Miyazono, K. (2011). Autocrine TGF- β protects breast cancer cells from
10 apoptosis through reduction of BH3-only protein, Bim. *J Biochem* 149, 55-65.

11 Hoshino, Y., Nishida, J., Katsuno, Y., Koinuma, D., Aoki, T., Kokudo, N., Miyazono, K., and Ehata, S. (2015).
12 Smad4 decreases the population of pancreatic cancer-initiating cells through transcriptional repression of
13 ALDH1A1. *Am J Pathol* 185, 1457-1470.

14